Pressure Measurement in the High Pressure Fuel System

Domenico Crescenzo

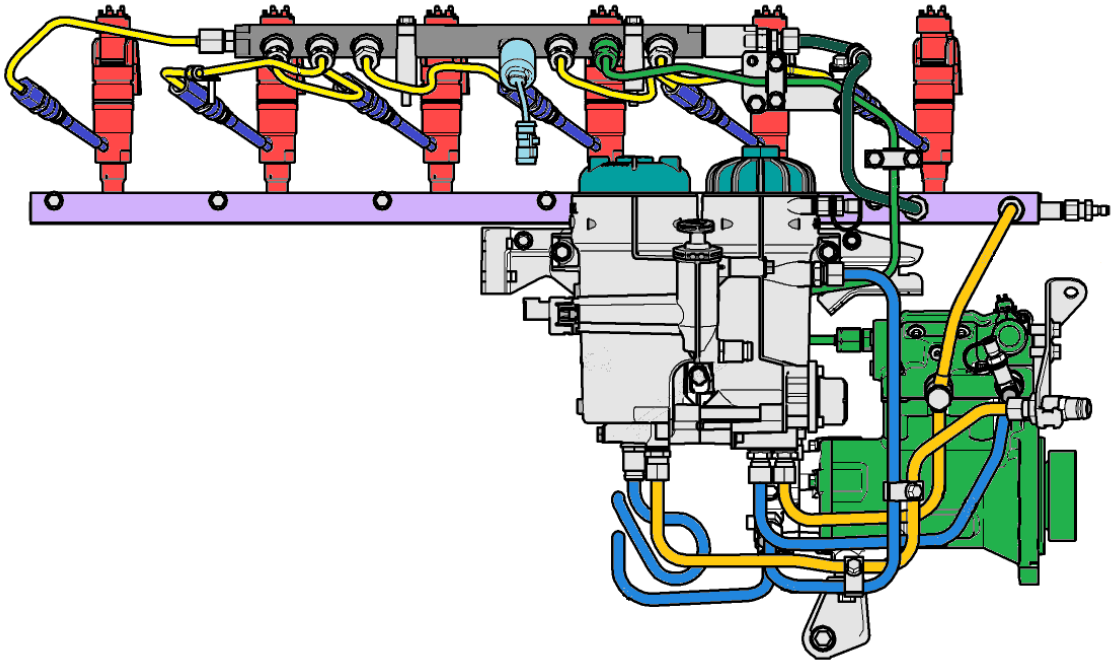

Master of Science Thesis MMK 2015:31 MFM 160
KTH Industrial Engineering and Management
Machine Design
SE-100 44 STOCKHOLM

Examensarbete MMK 2015:31 MFM 160

KTH Industriell teknik och management

Pressure Measurement in the High Pressure Fuel System

Domenico Crescenzo

Godkänt	Examinator	Handledare
	Dr. Andreas Cronhjort	Dr. Ola Stenlåås Dr. Andreas Cronhjort Mr. Erik Rundqvist Mr. Carlos Jorques Moreno
	Uppdragsgivare Scania CV AB	Kontaktperson Dr. Ola Stenlåås

Sammanfattning

För att uppnå den krävande utsläppslagstiftningen som ställs på dieselmotorer behövs en noggrannare styrning över insprutad bränslemängd i cylindern. En omfattande förståelse behövs över de viktigaste faktorerna som påverkar insprutningen. Faktorer som trycket i common rail-systemet, injektorernas faktiska öppningstid och temperaturen vid injektorn. Framförallt har common rail-trycket varit fokus i detta projekt: En exakt skattning av bränsletrycket är nödvändig för korrekt bestämning av injektionstiden vilket leder till förbättrad reglering av insprutat bränsle. Railtrycket präglas dock av betydande fluktueringar som påverkar mätningen. Experiment har utförts på en Scania D13 motor för att karaktärisera och öka förståelsen för railtryckssignaturen i statiska arbetspunkter: Trycksignalen består av överlagrad information från injektorerna, pumpslag och water-hammer störningar som tillsammans bildar ett komplext mönster som diskuteras ingående. Ett försök har gjorts att modellera de snabba transienterna i trycket: Frekvensinnehållet modelleras korrekt, men resultatet i tidsdomän avviker i både amplitud och fas jämfört med experimentell data. Slutligen har strategin som används för att skatta railtrycket idag på Scania CV AB undersökts och dess noggrannhet utretts. Baserat på kunskapen som erhållits har en ny, adaptiv mätteknik föreslagits. Den gör det möjligt att ändra estimeringstekniken beroende på motorns arbetspunkt. Metodens potential bevisas genom att ökad noggrannhet erhålls för insprutad bränslemängd vid statiska arbetspunkter. Dock krävs ytterligare utredning om metodens applicerbarhet vid transienta förlopp i motorn.

KTH Industrial Engineering and Management

Master of Science Thesis MMK 2015:31 MFM 160

Pressure Measurement in the High Pressure Fuel System

Domenico Crescenzo

Approved	Examiner	Supervisor
	Dr. Andreas Cronhjort	Dr. Ola Stenlåås Dr. Andreas Cronhjort Mr. Erik Rundqvist Mr. Carlos Jorques Moreno
	Commissioner	Contact person
	Scania CV AB	Dr. Ola Stenlåås

Abstract

In order to meet the demanding legislations on diesel engines exhaust emissions, an always more accurate control over the amount of fuel injected in the cylinders is required. A comprehensive understanding of the main factors involved in the injection process, therefore, should be achieved. Such factors are the pressure in the common rail, the injection ontime and the temperature at the injector. The rail pressure, in particular, has been the focus of this project: Its accurate acquisition is crucial for the correct determination of the injection duration and, consequently, for an improved control over the amount of fuel injected. The rail pressure, however, is characterized by significant instabilities affecting the measurement. An experimental campaign has been conducted on a Scania D13 engine in order to characterize and understand the rail pressure signature during engine steady operations: The superposition of injections, pump strokes and water-hammer instabilities forms a complex pattern extensively discussed. An attempt to model the pressure fast transients has been made: While the frequency content of the phenomenon investigated is correctly interpreted, the results obtained in the time domain diverge significantly in amplitude and phase from the experimental data collected. Finally, the measurement strategy adopted today at Scania CV AB to acquire the rail pressure has been investigated and its accuracy assessed. On the basis of the knowledge achieved, a new adaptive measurement technique, capable of changing the estimation process accordingly to the engine operating condition detected, is proposed. The potentiality of an increased accuracy in controlling the amount of fuel injected is proved for engine steady operations. Further investigation regarding the method tolerance to engine transients, however, is required.

ACKNOWLEDGEMENTS

"Obstacles are those frightful things you see when you take your eyes off your goal"

Henry Ford

With this project I am closing a long phase of my life where all the choices I made determined the man that I am today and will have a great influence in shaping the man that I will be tomorrow. I want to use this chance to thank all the people who crossed my path in the past years and who contributed to my personal and professional growth.

I want to thank Scania CV AB for providing me with all the support necessary to bring my work to relevant conclusions.

I thank my industrial supervisor, Dr Ola Stenlåås, for all I received in the past year: I will bring in my career each of the lessons I have drawn and this, I am confident, will let me be a better professional. I thank my academic supervisor, Dr Andreas Cronhjort, whose great experience was crucial in determining several key aspects of the presented project.

I want to thank both NESC and NESB groups, in particular Erik Rundqvist, who guided me through the complex features of the system I investigated. He gave me full access to his work, as Carlos Jorques Moreno did, who I want to thank for the constant support throughout the project. I want to express my gratitude to Mikael Nordin also, who was of great help in setting the experimental campaign. Several of the findings I achieved would have been impossible without the help of the NMCH group, therefore I must thank in particular Tomas Flink, Andreas Andersson and Martin Yakob.

Thanks to all the thesis workers who shared difficulties, challenges and successes of this experience in Scania with me: Mikael Gustafsson, Tobias Johansson, Tobias Rosvall, Christian Rugland and Maryam Shoe.

I want to mention my dear friends Matteo, Walter and Matteo for just being my family in these years abroad.

I thank the most amazing person I have ever met in my life, my girlfriend Martina, who never left my side and held my hand tight every time I felt lost: You are the source of my strength.

Ed infine, come non ringraziare la mia meravigliosa famiglia per il costante ed incondizionato appoggio garantitomi in questi anni. Guardo a voi oggi con gli occhi di un uomo e a voi guarderò sempre come esempio nella mia vita futura: Non abbandonate il mio fianco perché avrò sempre bisogno del vostro sostegno e consiglio.

Con amore,

Domenico

NOMENCLATURE

Notations

Symbol	Description
a	Wave speed (m/s)
A	Pipe cross sectional area (m)
ds	Incremental pipe length (m)
dV	Incremental pipe volume (m^3)
dW	Fluid weight of the control volume (Kg)
D	Pipe diameter
e	Wall thickness (m)
E	Young modulus (Pa)
f	Darcy-Weisbach friction coefficient (-)
K_T	Isothermal bulk modulus (Pa)
m_{f_req}	Fuel requested by the ECU (kg)
p	Flow pressure (Pa)
$P_{available}$	Rail pressure available in the ECU (bar)
Re	Reynolds number (-)
$T_{available}$	Rail temperature available in the ECU (K)
TDC	Cylinder Top Dead Centre (0°)
t_{inj}	Injection ontime (s)
V	Flow speed (m/s)
V_{main}	Injected fuel during main injection (mm^3)
V_{pil}	Injected fuel during pilot injection (mm^3)
ε	Pipe surface roughness (μm)
ε_2	Circumferential pipe strain (-)
θ	Local pipe slope (rad)
λ	Lagrange multiplier (-)
μ	Poisson ratio (-)
ρ	Fuel density (Kg/m^3)
σ_1	Pipe longitudinal stress (Pa)
σ_2	Pipe circumferential stress (Pa)
τ	Wall shear stress (N/m^2)

Abbreviations

CAD	Crank Angle Degree
CR	Common Rail
DT	Dwell Time
ECU	Engine Control Unit
EOI	End Of Injection
EOTTL	Electrical End Of Injection
FTCS	Forward in Time Central in Space
HPC	High Pressure Connector
HPP	High Pressure Pump
IMV	Inlet Metering Valve
LPP	Low Pressure Pump
MDV	Mechanical Damp Valve
MOC	Method of Characteristics
ODE	Ordinary Differential Equation
PDE	Partial Differential Equation
SOI	Start Of Injection
SOTTL	Electrical Start Of Injection

TABLE OF CONTENTS

1 INTRODUCTION AND BACKGROUND

This chapter describes the background of the presented project: Focus is given in particular to the importance of fuel injection systems and to the actual related challenges. Finally, the project goals and delimitations are presented.

1.1 Introduction

The Common Rail (CR) diesel fuel injection system plays a major role in the success of diesel engines in the European automotive market [1]. It decouples the pressure generation in the rail, and therefore the engine speed and load, from the actual injection process [2]. This results in an increased flexibility providing a high degree of freedom for the most important injection parameters. Rail pressure, injection ontime and number of injections can be optimized independently from the engine speed in order to guarantee a better control over the amount of fuel injected, leading to an improved efficiency and lower emissions [3]. The fuel injection process influences the fuel atomization, fuel-air mixing, mixture ignition, combustion and pollutant formation, hence it can be considered the most important flow process in diesel engines [4].

In order to meet the demanding legislations on exhaust emissions, however, an always more accurate control over the amount of fuel injected is required. This means that a comprehensive understanding of the main factors involved should be achieved. Such factors are the rail pressure, the injection ontime and the temperature at the injector. The main control challenge, in particular, is to precisely control the injected fuel quantity with respect to the rail pressure pulsations caused by the injection process [3].

Given the difficulties in controlling the rail pressure due to its fast transients, the purpose of this project is to understand, interpret and predict the pressure behaviour during the injection process. The understandings achieved will be source for suggested improvements in the rail pressure control.

1.2 The High Pressure Fuel System

The key component of the fuel injection system is the high pressure accumulator, or common rail. As shown in Figure 1, The common rail is designed to host fuel supplied by the high pressure fuel pump (HPP). The HPP is a positive displacement pump driven by the engine camshaft. The amount of fuel that it delivers to the rail is controlled through the inlet metering valve (IMV) whose task is to keep the requested rail pressure approximately constant. If faults in the system prevent the IMV from controlling the pressure level in the rail, the opening of the mechanical dump valve (MDV) allows the fuel to flow in the collector and guarantees a safe margin over the maximum pressure in the system. In a D13 Scania engine, six pipes connect the rail to the injectors through the high pressure connectors (HPC). Injectors are electronically controlled by the ECU that commands the electrical start and end of injection (respectively SOTTL and EOTTL). The actual start of injection (SOI) and end of injection (EOI) will be delayed due to the finite time response of the injector.

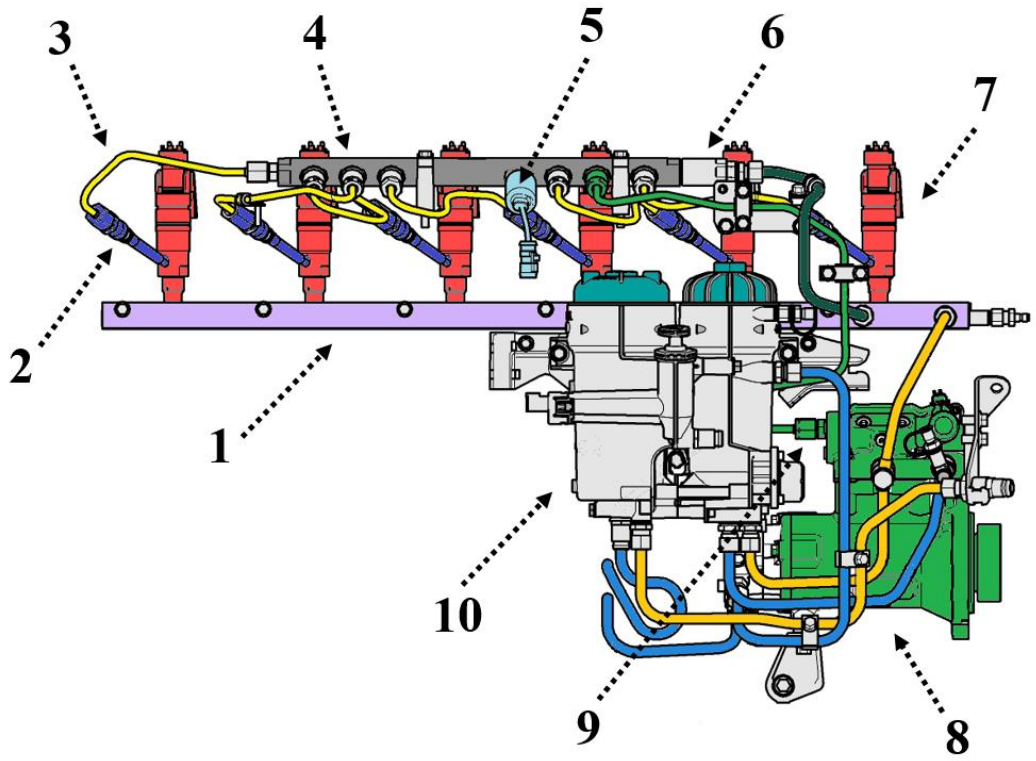

Figure 1 – Components of the high pressure fuel system are shown: fuel collector (1), HPC (2), fuel pipe (3), common rail (4), pressure sensor (5), mechanical damp valve (6), injector (7), low pressure and high pressure fuel pump (8), inlet metering valve (9), fuel filters (10) *[5]*.

1.3 Pressure Pulsations in the System

The accuracy of the injected fuel quantities is adversely affected by the fuel pressure pulsation. This excitation is induced by the high-speed flows in and out of the accumulator [3].

The flow entering the common rail is provided by the high pressure pump (HPP), driven by the engine camshaft and first source of pressure pulsations. The second major source of pulsations has its origins in the rapid opening and closing cycles of the injectors [6].

In Figure 2, experimental data from [7] is presented: The pressure instabilities at the rail pressure sensor - red line - and at the injector - blue line - are shown for one complete single injection cycle. The injected mass flow rate and the electrical current input are also reported.

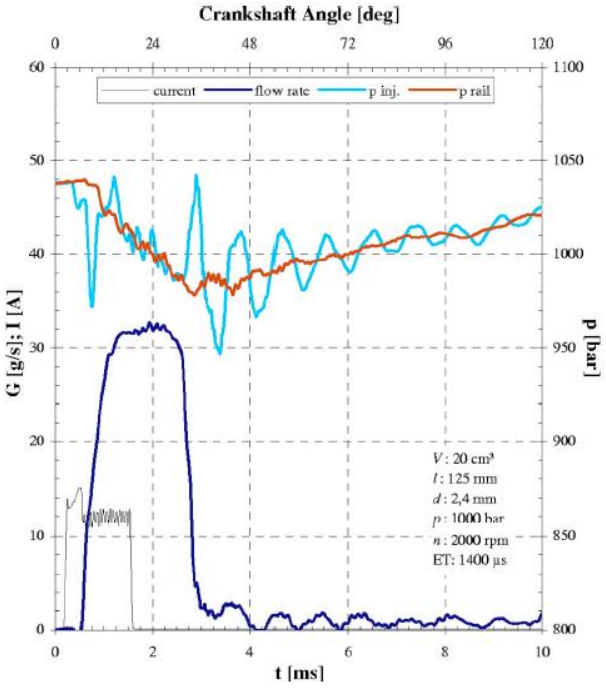

Figure 2 – Pressure instabilities at the rail pressure sensor - red line - and at the injector - blue line - are shown for one complete single injection cycle. The injected mass flow rate and the electrical current input are also reported. Note the oscillations in the amount of fuel delivered due to the pressure pulsations at the injector *[7]*.

In Figure 3a, the opening phase of the injection process is pictured closely. The pressure drop at the injector inlet, marked with *1* can be ascribed to the rarefaction wave set off by the sudden opening of the injector pilot valve, immediately after the current input. The rarefaction wave, travelling along the pipe, affects the rail pressure, which undergoes a slight drop in *1'*. The delay between *1* and *1'* is due to the finite propagation speed of the rarefaction wave. The opening of the pilot valve is followed by the actual fuel injection, source of a second rarefaction wave responsible for the drops in *2*, at the injector, and in *2'* in the rail. In the rail, this is reflected as a compression wave, determining the pressure rise in *4*.

Figure 3b depicts the effects of the compression wave following the sudden closure of the injector: A water-hammer effect, responsible for the steep pressure increase in *5*, is generated.

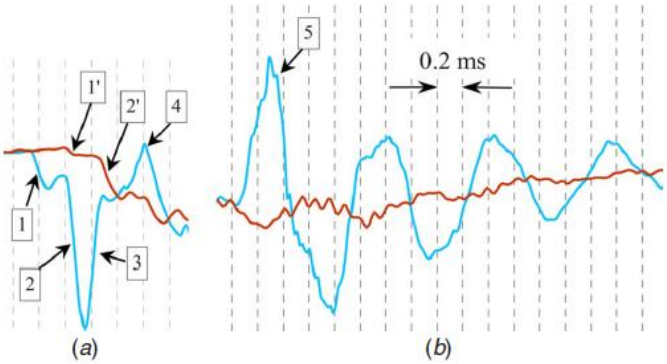

Figure 3a – Pressure instabilities at the rail pressure sensor - red line - and at the injector - blue line. the injector opening is source for rarefaction waves, responsible for the pressure drop measured. These waves are reflected as compression waves in the rail, responsible for the pressure increase in *4*.

Figure 3b – Pressure instabilities at the rail pressure sensor - red line - and at the injector - blue line. the rapid injector closure causes the water-hammer effect, transient phenomenon source of large oscillations in pressure.

A hydraulic transient is recognized as water-hammer if the flow velocities change so rapidly that the elastic properties of the pipe and liquid must be considered. In this case, the fuel velocity is suddenly forced to zero due to the rapid closure of the injector. As a consequence the hydraulic head at the injector abruptly increases by an amount - See peak 5 in Figure 3b - just sufficient to reduce the momentum of the moving fuel to zero. The local rise in pressure causes a slight enlargement in the pipe and an increase in fuel density. A compression wave, propagating upstream, is generated [8]. The perturbation undergoes reflections propagating into the system until friction losses exhaust its kinetic energy into thermal losses [9], as Figure 3b suggests.

Due to wave propagations, some injectors are likely to open when the pressure in the system is at a local maximum while others when it is at a local minimum [6]. This produces significant fluctuations on the volume of fuel injected and puts a constraint to the capabilities of reducing the dwell time between two subsequent shots in a multiple injection sequence [7]. The pressure oscillations triggered by the pilot injection, for example, can have a remarkable influence on the subsequent main injection. Figure 4 shows the effect of the dwell time (*DT*) between pilot and main injections against the amount of fuel delivered. While the fuel delivered during the pilot injection (V_{pil}) remains approximately constant with the dwell time, V_{main} shows sensible variations as DT varies [1].

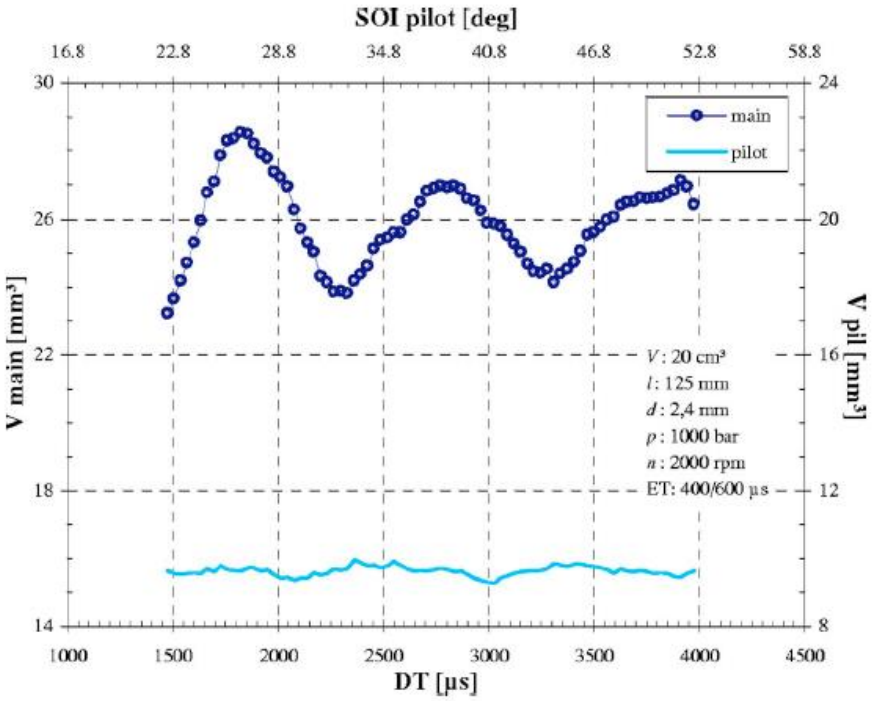

Figure 4 – Effect of the dwell time (DT) between pilot and main injections over the amount of fuel delivered during the main injection (V_{main}). While the fuel delivered during the pilot injection (V_{pil}) remains approximately constant with the dwell time, V_{main} shows sensible variations as DT varies *[1]*.

Pressure pulsations in the high pressure fuel system, therefore, are complex phenomena requiring important computational sources in order to be followed closely. The actual pressure sampling method implemented on the ECU is unable to catch the pressure fast transients hence, the control over the fuel injected has a limited accuracy.

1.4 Controlling the Rail Pressure

The main parameters involved in the injection process are shown in Figure 5. The amount of fuel requested and the values of rail pressure and temperature previously measured and available in the software (respectively $P_{available}$ and $T_{available}$) determine together the injection ontime. When the injector opens, however, the actual rail pressure and temperature may differ from $P_{available}$ and $T_{available}$. This results in an amount of fuel injected different from what the system requires.

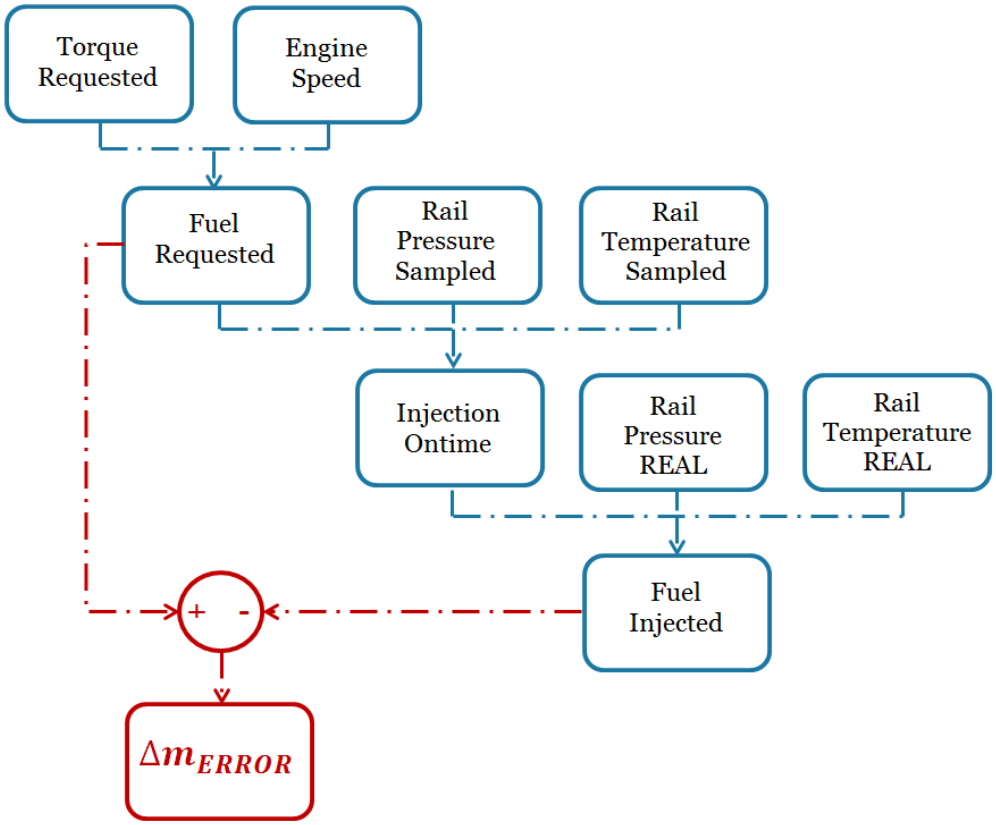

Figure 5 – The injection ontime is computed on the rail pressure and temperature previously measured and available in the software, which do not correspond to the actual pressure and temperature at the injector opening. This limits the accuracy over the control of the amount of fuel injected.

While the temperature has a minor effect due to its slow variations, the main source of error resides in the impossibility of accurately following the fast pressure transients. An optimization, therefore, is needed in order to minimize the differences between the rail pressure sensed by the software and the actual rail pressure at the injector opening.

1.5 Purpose – Problem Statement

Three main tasks have been identified for the present project:

1. Build a model able to predict and interpret the complex pressure transients in the high pressure fuel system. The contribution from the pump, the water-hammer effect, friction losses and the fuel compressibility should be taken into account.
2. Carry out an experimental investigation. Analyse and interpret the experimental results obtained. Verify the validity and the accuracy of the model. Evaluate pro and cons of the current sampling technique.
3. Based on the previous results, suggest improvements to optimize the sampling technique. When, how, how often to sample? How to process the information acquired?

1.6 Delimitations

Only steady engine operating points are investigated and modelled. The high pressure fuel system is assumed to be isothermal and the fuel flow one-dimensional along the pipeline. Wave reflections due to pipe turnings are not going to be considered.

2 ANALYTICAL APPROACH

The high pressure fuel system components form together a pipeline network: The common rail and the fuel lines from the HPP and to the injectors are modelled. The detailed analytical description of one fuel line is presented in this chapter.

2.1 Modelling Strategy

Fast transients characterize the fuel flow in the high pressure components of the fuel injection system [2]. The sudden closure of each injector causes a water-hammer instability propagating throughout the fuel line: In order to obtain an accurate characterization of the transient, the elasticity of both the pipe and the liquid should be considered in the analysis [8].

The flow is assumed to be one-dimensional everywhere in the system: Variations in fluid or flow properties along the cross section are disregarded. References [10] and [11] supports the validity of the unidirectional approach when studying water-hammer problems in pipe systems.

2.2 Conservation of Momentum

The analysis of transient flows requires the application of the momentum conservation law. The forces acting on a cylindrical fluid element are shown in Figure 6, where contributions due to the pressure (p), the wall shear stress (τ) and the fluid weight (dW) are reported.

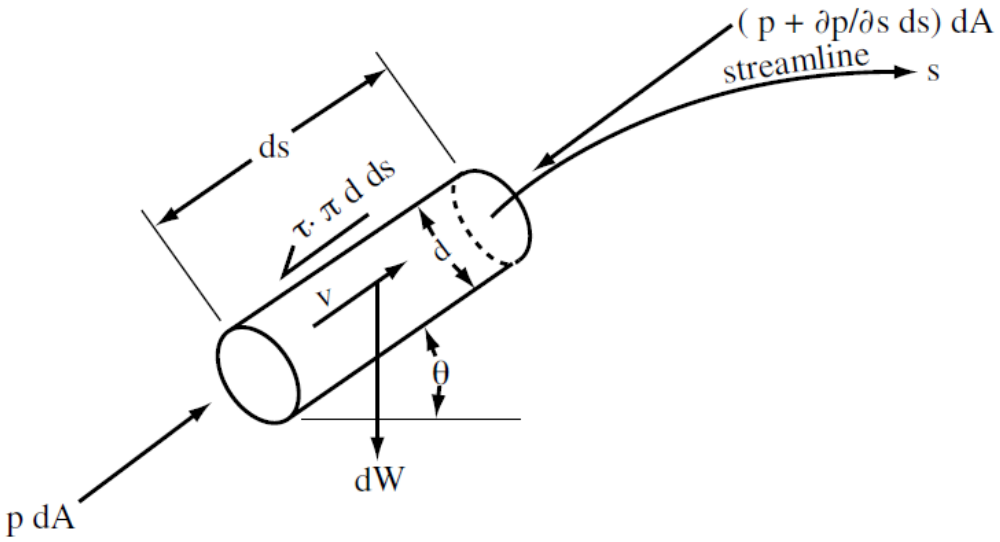

Figure 6 – Forces over a cylindrical fluid element are shown. Contributions due to fluid pressure (pdA *and* $\left(p+\frac{\partial p}{\partial s}ds\right)dA$), wall shear stress ($\tau\pi dds$) and fluid weight ($dW$) are reported *[8]*.

Along the streamline direction *s*, Newton's second law gives Equation (1).

$$\sum F_s = ma_s = m\frac{dV}{dt} \qquad (1)$$

Where m is the fluid mass in the control volume and dV/dt is the total derivative of the fluid velocity. By substituting the forces shown in Figure 8 in Equation (1), the following is obtained.

$$pdA - \left(p + \frac{\partial p}{\partial s} ds\right) dA - dW \sin\theta - \tau \pi D(ds) = \frac{dW}{g} \frac{dV}{dt} \qquad (2)$$

In the system, the effect of local pipe slopes is negligible if compared to the contribution given by the pressure or the viscous losses. Hence, $dW \sin\theta$ will be disregarded.
Dividing Equation (2) by $dW = \rho g \pi D^2 ds$, the one-dimensional Euler equation is obtained.

$$-\frac{1}{\rho g} \frac{\partial p}{\partial s} - \frac{4\tau}{\rho g D} = \frac{1}{g} \frac{dV}{dt} \qquad (3)$$

Every component in the system is assumed to be perfectly cylindrical, therefore the wall shear stress τ can be expressed in terms of the Darcy-Weisbach friction factor f [8], accordingly to Equation (4).

$$\tau = \frac{1}{8} f \rho V |V| \qquad (4)$$

The definition of the friction factor f accounts for a quasi-steady and an unsteady contributions from the transient flow [12]:

$$f = f_q + f_u \qquad (5)$$

Modelling of transients events in pipelines, however, has historically been performed using a quasi-steady state friction approximation only, sufficient to achieve an acceptable match with experimental data [13]. For this reason, in the present project only f_q is modelled ($f = f_q$).

The quasi steady friction factor is closely coupled to the flow Reynolds number (Re) and to the pipe surface roughness (ε): This relationship has three different regions of application [14]. In the laminar flow region, where $Re < 2100$:

$$f = \frac{64}{Re} \qquad (6)$$

For higher Reynolds number ($Re > 4000$), the Colebrook-White equation for turbulent flow should be employed:

$$\frac{1}{\sqrt{f}} = -2 \log_{10}\left(\frac{\varepsilon}{3.7D} + \frac{2.51}{Re\sqrt{f}}\right) \qquad (7)$$

The Colebrook-White equation, however, is implicit. An explicit formulation for the turbulent quasi-steady friction factor is provided by Swamee and Jain [15]:

$$f = \left\{2 \log_{10}\left[\frac{\varepsilon}{3.7D} + \left(\frac{6.97}{Re}\right)^{0.9}\right]\right\}^{-2} \qquad (8)$$

The third region is characterized by a transitional flow ($2100 < Re < 400$) where the quasi steady friction coefficient can be linearly interpolated from Equation (6) and Equation (8).

Equation (4) gives the momentum conservation for a transient one-dimensional flow [8]:

$$\frac{dV}{dt} + \frac{1}{\rho} \cdot \frac{\partial p}{\partial s} + \frac{f}{2D} V|V| = 0 \qquad (9)$$

2.3 Conservation of Mass

The control volume employed for the following analysis coincides with the inner volume of a pipe segment *ds*, as Figure 7 shows.

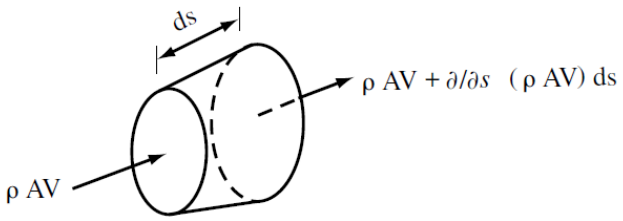

Figure 7 – Control volume coinciding with the interior surface of the pipe *[8]*.

Equation (10) gives an expression for the conservation of mass in the control volume under analysis.

$$\rho AV - \left[\rho AV + \frac{\partial}{\partial s}(\rho AV)ds\right] = \frac{\partial}{\partial t}(\rho A ds) \qquad (10)$$

Expanding the parenthesis, regrouping and dividing by the control volume mass ρAV leads to Equation 11.

$$\frac{1}{\rho}\left(\frac{\partial \rho}{\partial t} + V\frac{\partial \rho}{\partial s}\right) + \frac{1}{A}\left(\frac{\partial A}{\partial t} + V\frac{\partial A}{\partial s}\right) + \frac{1}{ds}\frac{\partial}{\partial t}(ds) + \frac{\partial V}{\partial s} = 0 \qquad (11)$$

Since time and convective derivatives of the density and of the pipe section can be expressed as:

$$\frac{\partial \rho}{\partial t} + V\frac{\partial \rho}{\partial s} = \frac{d\rho}{dt} \qquad (12)$$

$$\frac{\partial A}{\partial t} + V\frac{\partial A}{\partial s} = \frac{dA}{dt} \qquad (13)$$

Equation (11) becomes:

$$\frac{1}{\rho}\frac{d\rho}{dt} + \frac{1}{A}\frac{dA}{dt} + \frac{1}{ds}\frac{\partial}{\partial t}(ds) + \frac{\partial V}{\partial s} = 0 \qquad (14)$$

Where dA/dt accounts for the elastic pipe bulge caused by the pressure wave passage.

A model for the pressure pulsations in the high pressure fuel system is the project first goal, therefore the conservation of mass should be expressed in terms of pressure *p*. In order to simplify this task, the system will be considered isothermal. Limitations due to this assumption will be discussed in a later stage.

Consequently, the fluid bulk modulus (K) can be expressed as [8]:

$$K = -\frac{dp}{dV/V} = \frac{dp}{d\rho/\rho} = K_T \quad (15)$$

Leading to Equation (16):

$$\frac{1}{\rho}\frac{d\rho}{dt} = \frac{1}{K_T}\frac{dp}{dt} \quad (16)$$

Where K_T is the isothermal bulk modulus.

The elastic pipe bulge dA/dt can be expressed in terms of pressure p also. Two further assumptions, however, are required: The pipe is fully restrained from axial movements, i.e. deformations take place in the cross-sectional area only, and a thin-walled pipe is considered. A thin-walled pipe implies $D/e < 40$, where e is the wall thickness [8]. This requirement does not apply to the actual fuel line, therefore this assumption will be relaxed in a later stage.

The change in pipe volume V caused by circumferential stretching is given by Equation (17) [8].

$$dV = \pi D \frac{dD}{2} dL \quad (17)$$

Since

$$dD = D d\varepsilon_2 \quad (18)$$

Where $d\varepsilon_2$ represents the circumferential pipe strain, Equation (17) becomes:

$$dV = \frac{1}{2}\pi D^2 dL d\varepsilon_2 \quad (19)$$

Elastic deformations in the cross-sectional are:

$$dA = \frac{dV}{dL} = \frac{1}{2}\pi D^2 d\varepsilon_2 \quad (20)$$

According to [8], the circumferential pipe strain can be expressed as:

$$d\varepsilon_2 = \frac{d\sigma_2 - \mu d\sigma_1}{E} \quad (21)$$

Where $d\sigma_2$ is the mechanical stress along the circumferential direction, $d\sigma_1$ the mechanical stress along the pipe axis direction, μ the Poisson's ratio and E the material Young modulus. Combining Equation (20) and Equation (21):

$$\frac{1}{A}dA = \frac{2}{E}(d\sigma_2 - \mu d\sigma_1) \quad (22)$$

The pipe is fully restrained from axial movements, therefore no deformations along the pipe axis direction take place and the following relations hold [8]:

$$d\sigma_1 = \mu d\sigma_2 \quad (23)$$

$$d\sigma_2 = \frac{D}{2e} dp \quad (24)$$

Finally,

$$\frac{1}{A}\frac{dA}{dt} = (1-\mu^2)\frac{D}{eE}\frac{dp}{dt} \qquad (25)$$

Including Equation (25) and Equation (16) in Equation (11):

$$\frac{1}{K_T}\frac{dp}{dt} + (1-\mu^2)\frac{D}{eE}\frac{dp}{dt} + \frac{1}{ds}\frac{\partial}{\partial t}(ds) + \frac{\partial V}{\partial s} = 0 \qquad (26)$$

Considering that:

$$\frac{1}{ds}\frac{\partial}{\partial t}(ds) = 0 \qquad (27)$$

for the pipe axial constraint, Equation (26) becomes:

$$\frac{1}{K_T}\frac{dp}{dt} + (1-\mu^2)\frac{D}{eE}\frac{dp}{dt} + \frac{\partial V}{\partial s} = 0 \qquad (28)$$

Rearranging Equation (28):

$$\frac{dp}{dt} = \left[\frac{1}{K_T} + (1-\mu^2)\frac{D}{eE}\right] + \frac{\partial V}{\partial s} = 0 \qquad (29)$$

According to [8], the wave speed a in an elastic pipe is defined as:

$$a^2 = \frac{1}{\rho\left[\frac{1}{K_T} + C\cdot\frac{D}{eE}\right]} \qquad (30)$$

Where the constant C for a thin-walled pipe is:

$$C = (1-\mu^2) \qquad (31)$$

Combining Equation (29) and Equation (30), the conservation of mass can be finally expressed as:

$$a^2\frac{\partial V}{\partial s} + \frac{1}{\rho}\frac{dp}{dt} = 0 \qquad (32)$$

As mentioned before the assumption of thin-walled pipe does not apply to the actual fuel line. In order to model a thick-walled pipe, the constant C must be modified accordingly to Equation (33) [8]:

$$C = \frac{1}{1+{}^{e}/_{D}}\cdot\left[(1-\mu^2) + 2\frac{e}{D}(1-\mu^2)(1+\frac{e}{D})\right] \qquad (33)$$

2.4 System of Equations

In Section 2.2 and 2.3, equations for the conservation of momentum and mass have been obtained. These relations account for both time and space variations in speed and pressure:

$$\begin{cases} \frac{dV}{dt} + \frac{1}{\rho}\cdot\frac{\partial p}{\partial s} + \frac{f}{2D}V|V| = 0 \\ a^2\frac{\partial V}{\partial s} + \frac{1}{\rho}\frac{dp}{dt} = 0 \end{cases} \qquad (34)$$

Space-varying terms, however, are in general much less significant in determining the solution behavior than are the time-varying terms [8]. Therefore, the following computational model will be developed on approximate equations obtained by neglecting the spatial variation of *p* and *V*, as the system of Equations (35) shows.

$$\begin{cases} \frac{\partial V}{\partial t} + \frac{1}{\rho} \cdot \frac{\partial p}{\partial s} + \frac{f}{2D} V|V| = 0 \\ a^2 \frac{\partial V}{\partial s} + \frac{1}{\rho} \frac{\partial p}{\partial t} = 0 \end{cases} \qquad (35)$$

This assumption results in a great simplification in the numerical procedure adopted to solve the system.

3 NUMERICAL METHOD

The method of characteristics is presented and adapted to the actual system under analysis. An extensive explanation regarding the boundary conditions designed for the model is given.

3.1 Method of Characteristics (MOC)

Among the numerical techniques developed to approximate the solutions of the 1D water-hammer equations, the method of characteristics (MOC) is the most popular due to its desirable attributes of accuracy, simplicity and numerical efficiency [16]. The essence of the method of characteristics is the successful replacement of a pair of partial differential equations by an equivalent set of ordinary differential equations (ODE) [8].

A linear and constant Lagrange multiplier (λ) able to satisfy the linear combination of the system of Equations (35) is introduced:

$$\lambda\left(\frac{\partial V}{\partial t}+\frac{1}{\rho}\frac{\partial p}{\partial s}+\frac{f}{2D}V|V|\right)+\left(a^2\frac{\partial V}{\partial s}+\frac{1}{\rho}\frac{\partial p}{\partial t}\right)=0 \qquad (36)$$

Regrouping terms,

$$\left(\lambda\frac{\partial V}{\partial t}+a^2\frac{\partial V}{\partial s}\right)+\left(\frac{1}{\rho}\frac{\partial p}{\partial t}+\frac{\lambda}{\rho}\frac{\partial p}{\partial s}\right)+\frac{\lambda f}{2D}V|V|=0 \qquad (37)$$

In order to obtain a set of ordinary differential equations, the Lagrange multiplier should be selected so that the material derivative of *P* and *V* is obtained [17]. Therefore:

$$\lambda\frac{DV}{Dt}=\lambda\frac{\partial V}{\partial t}+\lambda\frac{ds}{dt}\frac{\partial V}{\partial s}=\lambda\frac{\partial V}{\partial t}+a^2\frac{\partial V}{\partial s} \qquad (38)$$

$$\frac{1}{\rho}\frac{Dp}{Dt}=\frac{1}{\rho}\frac{\partial p}{\partial t}+\frac{1}{\rho}\frac{ds}{dt}\frac{\partial p}{\partial s}=\frac{1}{\rho}\frac{\partial p}{\partial t}+\frac{\lambda}{\rho}\frac{\partial p}{\partial x} \qquad (39)$$

Equation (38) and Equation (39) set constraints over λ:

$$\begin{cases}\lambda=\frac{ds}{dt}\\ \lambda^2=a^2\end{cases} \qquad (40)$$

Resulting in:

$$\lambda=\pm a \qquad (41)$$

The Lagrange multiplier remains constant as long as the wave speed is constant. This does not apply in the actual fuel system due to temperature gradients and different inner diameters of the rail and the fuel lines. The system, however, is considered isothermal and the variation of *a* due to diameter variations is disregarded.

Two different values for the Lagrange multipliers lead to two different ordinary differential equations:

$$\frac{dV}{dt}+\frac{1}{a\rho}\frac{dp}{dt}+\frac{f}{2D}V|V|=0 \quad if \quad a=\frac{ds}{dt} \qquad (42)$$

$$\frac{dV}{dt} - \frac{1}{a\rho}\frac{dp}{dt} + \frac{f}{2D}V|V| = 0 \quad if \quad a = -\frac{ds}{dt} \qquad (43)$$

Since special relations must be maintained between s and t in Equation (42) and Equation (43), $a = ds/dt$ and $a = -ds/dt$ are called *characteristics* of Equation (42) and Equation (43). In particular , $a = ds/dt$ is known as C^+ characteristic, while $a = -ds/dt$ as C^- characteristic [8].

$$C^+ : \quad a = \frac{ds}{dt} \qquad (44)$$

$$C^- : \quad a = -\frac{ds}{dt} \qquad (45)$$

Integrating the characteristics leads to:

$$C^+ : \quad t = \frac{s}{a} + const \qquad (46)$$

$$C^- : \quad t = -\frac{s}{a} + const \qquad (47)$$

Equations (46) and (47) describe a family of straight lines of slope $1/a$ and $-1/a$ on the *s-t* plane, shown in Figure 8.

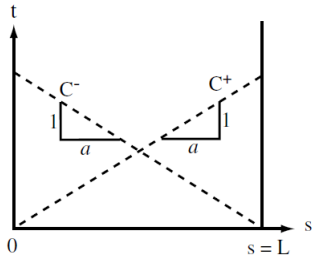

Figure 8 – Characteristic lines on the *s-t* plane *[8]*.

Along the characteristic lines C^+ and C^-, Equations (42) and (43) hold. As Figure 9 shows, the intersection of two characteristic lines determines univocally a point *P* in the *s-t* plane. The power of the method employed lays in this: Each point in space and time can be univocally determined on the time-space grid - characteristic grid - built by the intersection of the characteristic lines. The choice of a time step for the simulation will determine the space discretization and, therefore, the grid density.

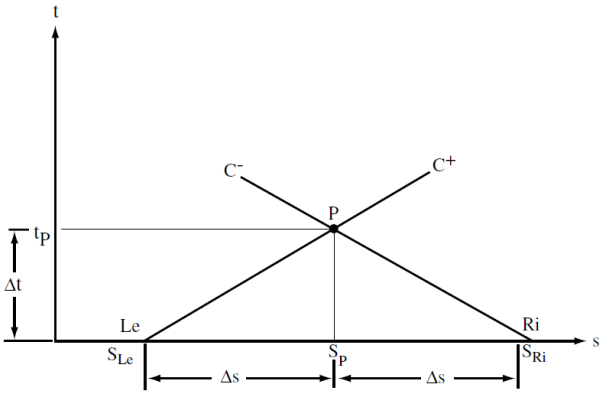

Figure 9 – Forward in Time Central in Space (FTCS) numerical scheme is adopted. The numerical solution travels along the characteristic lines C^+ and C^- *[8]*.

The numerical solution of the system travels along each characteristic line accordingly to a FTCS scheme (Forward in Time Central in Space). The finite difference representation is:

$$C^+ \;:\; \left(V_p - V_{Le}\right) + \frac{g}{a}\left(H_p - H_{Le}\right) + \frac{f\Delta t}{2D} V_{Le}|V_{Le}| \qquad (48)$$

$$C^- \;:\; \left(V_p - V_{Ri}\right) - \frac{g}{a}\left(H_p - H_{Ri}\right) + \frac{f\Delta t}{2D} V_{Ri}|V_{Ri}| \qquad (49)$$

The numerical scheme adopted is capable of picturing the initial response of the system accurately. However, it fails in solving the decay stage of the phenomenon revealing all the limits of the approach employed. Although several more advanced numerical approaches have been attempted ([16]), the accuracy achieved with the method of characteristics suffices for the purposes of this work.

3.2 Multi-Zone Model

A multi-zone model approach is adopted. The characteristic grid, in particular, is extended among the sub-systems shown in Figure 10, i.e. the six fuel lines, the rail sections, the high pressure connectors and the fuel line connecting the HPP to the common rail.

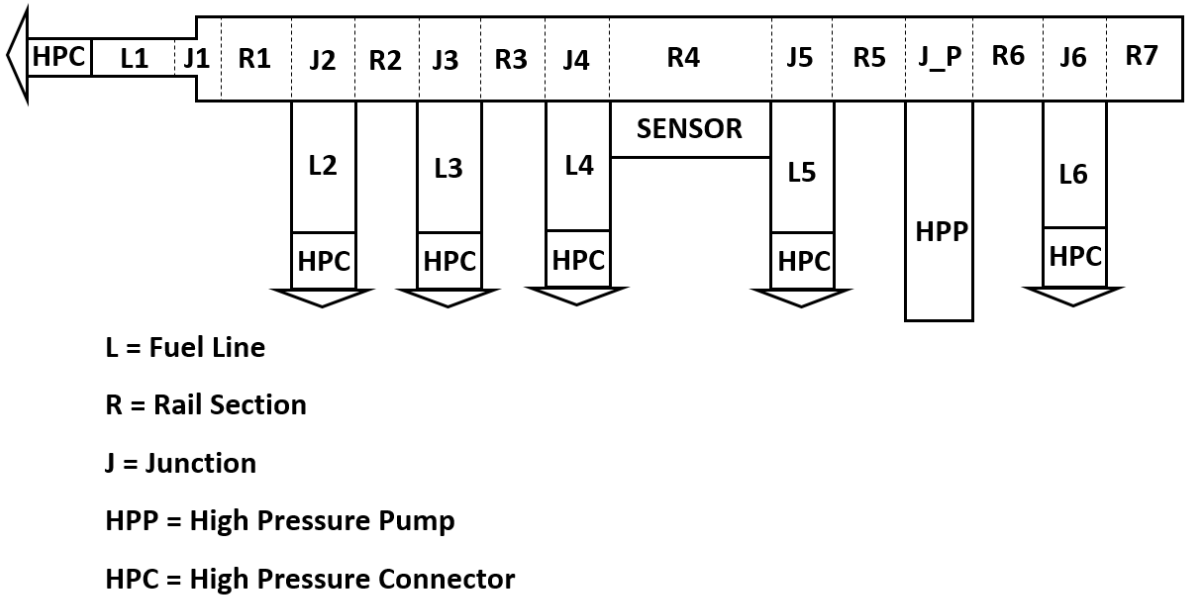

Figure 10 – The multi-zone model adopted. The characteristic grid is extended among the rail, the fuel lines and the high pressure connectors. Special attention should be given to the junctions J1-J6. Note the position of the virtual rail pressure sensor implemented in the model.

While the mentioned components are modelled according to what described in the previous section, special attention should be given to the junction sub-systems. At the junctions, the boundaries of the adjacent zones are determined and therefore more constraints apply.

Considering the two-way junction J1, the following relations hold:

$$\begin{cases} C^+ : \left(V^t{}_{L1(end)} - V^{t-1}{}_{L1(end-1)}\right) + \frac{g}{a}\left(H^t{}_{L1(end)} - H^{t-1}{}_{L1(end-1)}\right) + \frac{f\Delta t}{2D_L} V^{t-1}{}_{L1(end-1)} \left|V^{t-1}{}_{L1(end-1)}\right| \\ C^- : \left(V^t{}_{R1(1)} - V^{t-1}{}_{R1(2)}\right) - \frac{g}{a}\left(H^t{}_{R1(1)} - H^{t-1}{}_{R1(2)}\right) + \frac{f\Delta t}{2D_R} V^{t-1}{}_{R1(2)} \left|V^{t-1}{}_{R1(2)}\right| \end{cases} \quad (50)$$

Two additional equations are required in order to solve the system of Equations (50) in terms of $V^t{}_{L1(end)}$, $H^t{}_{L1(end)}$, $V^t{}_{R1(1)}$, $H^t{}_{R1(1)}$. These equations are the conservation of mass at the junction - Equation (51) - and the conservation of momentum - Equation (52):

$$V^t{}_{L1(end)} \cdot D_L^2 = V^t{}_{R1(1)} \cdot D_R^2 \quad (51)$$

$$H^t{}_{L1(end)} = H^t{}_{R1(1)} \quad (52)$$

In Equation (51), $D_L = 3\ mm$ and $D_R = 8\ mm$ are respectively the fuel line and rail internal diameters. In Equation (52), local losses in pressure head at the junction are assumed to be negligible. The complete system of equations for the two-way junction is:

$$\begin{cases} C^+ : \left(V^t{}_{L1(end)} - V^{t-1}{}_{L1(end-1)}\right) + \frac{g}{a}\left(H^t{}_{L1(end)} - H^{t-1}{}_{L1(end-1)}\right) + \frac{f\Delta t}{2D_L} V^{t-1}{}_{L1(end-1)} \left|V^{t-1}{}_{L1(end-1)}\right| \\ C^- : \left(V^t{}_{R1(1)} - V^{t-1}{}_{R1(2)}\right) - \frac{g}{a}\left(H^t{}_{R1(1)} - H^{t-1}{}_{R1(2)}\right) + \frac{f\Delta t}{2D_R} V^{t-1}{}_{R1(2)} \left|V^{t-1}{}_{R1(2)}\right| \\ V^t{}_{L1(end)} \cdot D_L^2 = V^t{}_{R1(1)} \cdot D_R^2 \\ H^t{}_{L1(end)} = H^t{}_{R1(1)} \end{cases} \quad (53)$$

With similar reasoning a system of equations for the three-way junctions can be obtained. For further details, see [8].

3.3 Initial and Boundary Conditions

The time marching method of characteristics requires both initial and boundary conditions in order to be fully operating.

At time $t = 0$, the system is assumed to be at rest, i.e. constant rail pressure, all injectors closed and no fuel delivered from the high pressure pump.

At the injectors, the fuel flow profile during the main injection is modelled, see Figure 11. As discussed in Section 1.4, the ECU commands the amount of fuel to be injected at each engine operating point. Based on the measured rail pressure available in the software, the injection ontime is determined. It is assumed in the model that the ECU commanded amount of fuel corresponds exactly to the actual fuel injected. A flow profile able to guarantee the discharge of this quantity in the settled injection ontime is then modelled in analogy with a real injection flow profile. The model, as well as the ECU, contains information regarding the pilot valve opening and closing delay (SOI and EOI), with respect to the electrical commands given (SOTTL and EOTTL). The firing order 1-5-3-6-2-4 of a Scania D13 engine is reproduced, see Figure 12.

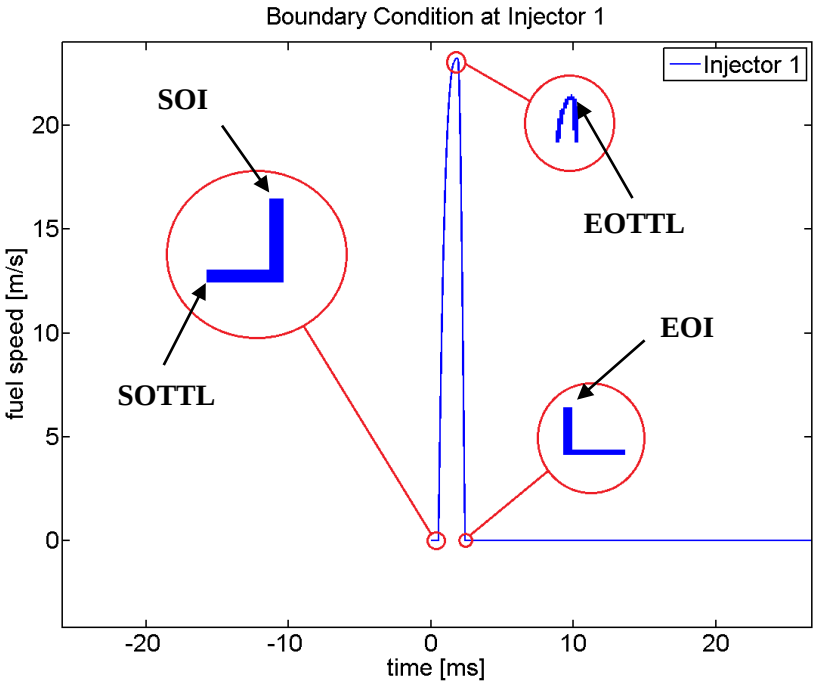

Figure 11 – Boundary condition at injector 1. The flow profile guarantees the injection of the commanded amount of fuel. Note the delays between the electrical start of injection (SOTTL) and the actual start of injection (SOI) and between the electrical end of injection (EOTTL) and the actual end of injection (EOI).

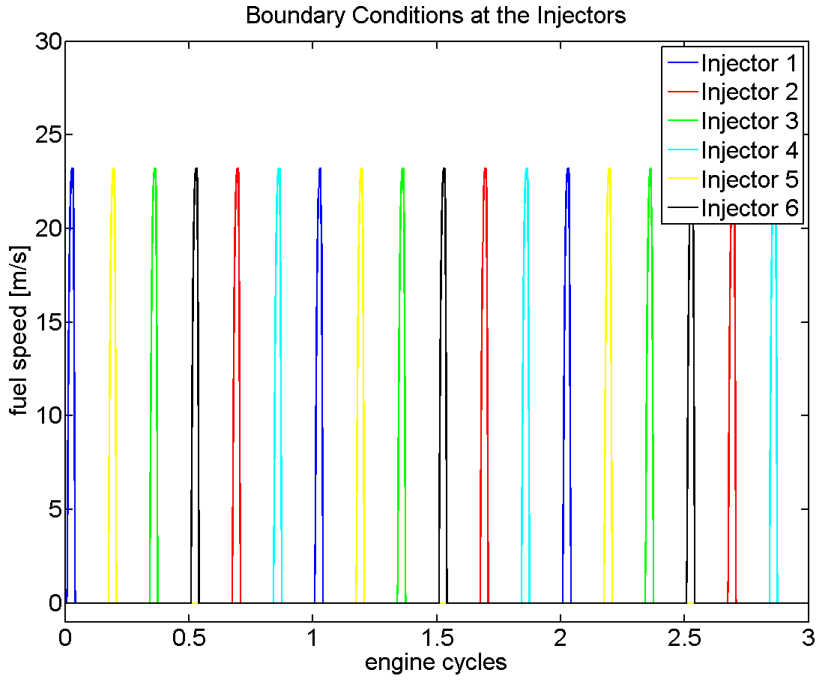

Figure 12 - Boundary conditions at the injectors. Each injector fires once per engine cycle, for a total number of six injections per engine cycle. A simplification is made and each injection takes place every 120 CAD. The firing order 1-5-3-6-2-4 of a Scania D13 engine is reproduced.

At the high pressure pump side, the fuel flow profile is shaped to counteract the pressure drops following the injections and keep the requested rail pressure approximately constant. In the actual system this task is attained by the IMV which controls the amount of fuel delivered to the rail. In the model, however, a mixed boundary condition on the fuel pressure and speed is implemented. The HPP is characterized by four strokes per crank shaft revolutions: In order to reproduce this behaviour, a trigger square wave is defined, see Figure 13. For the square wave being equal to one, the boundary condition is imposed on the fuel pressure, set at the requested constant rail level. Doing so, a pump stroke is simulated and the pressure drop due to the previous injections is balanced. For the square wave being equal to zero, the boundary condition is imposed on the flow speed, set at zero. During this phase no fuel is delivered from the HPP and the pressure drop during the injections is not counteracted.

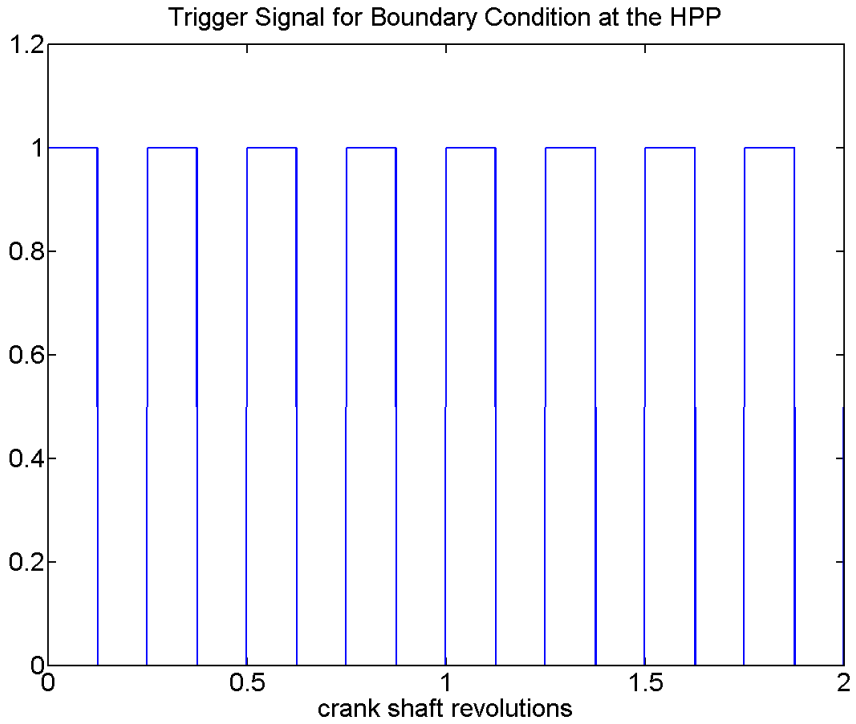

Figure 13 – Trigger signal for the boundary condition at the HPP. For the trigger signal being equal to one, a boundary condition on pressure is set to simulate the pump stroke. Note the frequency of four pump strokes per crank shaft revolution. For the trigger signal being zero, a boundary condition on flow speed is set. The speed is zero, i.e. no fuel is delivered from the HPP and the pressure drop during the injections is not counteracted.

4 EXPERIMENTAL SETUP

An experimental investigation is required in order to validate the model developed and achieve a better understanding over the system dynamics. Data from different tests have been employed in order to characterize the main sources of pulsations in the high pressure fuel system.

The pressure excitation in the high pressure fuel system is induced by the high-speed flows in and out of the accumulator [3]. The oscillations, therefore, originate from the superposition of the pulsating flow fed by the high pressure pump and the water-hammer effect due to the rapid opening and closing cycles of the injectors.

In order to accurately characterize the latter phenomenon, an experimental campaign has been conducted by the senior engineer Erik Rundqvist (NESB) at Scania CV AB. Specific tests with no pump contribution and no deflagration in the combustion chamber have been performed: The effect of a single fuel injection in terms of rail pressure oscillations has been investigated at different rail pressures and for different injected quantities [18]. Signals have been acquired through the pressure transducer currently in use for on-board applications and sampled at a frequency of 250 kHz.

A second experimental campaign has been conducted by the author in collaboration with Maryam Shoe and the CLCC group (Mikael Gustafsson, Tobias Johansson, Tobias Rosvall and Christian Rugland). Tests have been performed on a D13 Scania engine, shown in Figure 14. Focus of this research was the investigation of the pulsations generated by other possible sources, e.g. the high pressure pump strokes and the fuel deflagrations in the combustion chamber. The fuel employed was the standard Swedish Diesel.

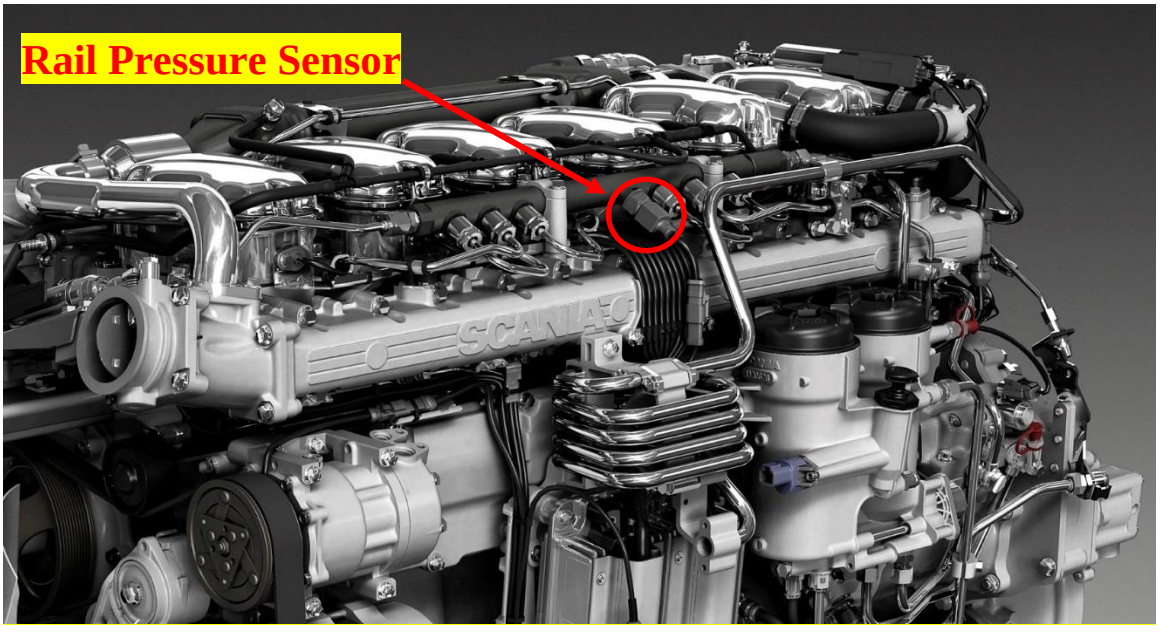

Figure 14 – Experimental setup: the Scania D13 engine is shown. Note the position of the standard rail pressure sensor.

Components of the high pressure fuel system can be divided in two main categories: Static components and dynamic ones. The geometrical features of the static components of the system tested are reported in Table 1:

Table 1 – Specifications regarding the static components of the high pressure fuel system.

Part	Part Number	Length (mm)	Diameter (mm)
Common Rail	2123671	470	8
Line to cylinder 1	1743982	290	3
Line to cylinder 2	1862547	325	3
Line to cylinder 3	1862548	300	3
Line to cylinder 4	1860539	300	3
Line to cylinder 5	2049355	300	3
Line to cylinder 6	1860541	300	3
HPC	1832724	145	3

Among the dynamic components of the system, special attention is given to the high pressure pump and to the injectors. As shown in Figure 15, the HPP - part number 2007109 - is a positive displacement pump characterized by two plungers of 6 *mm* diameter each.

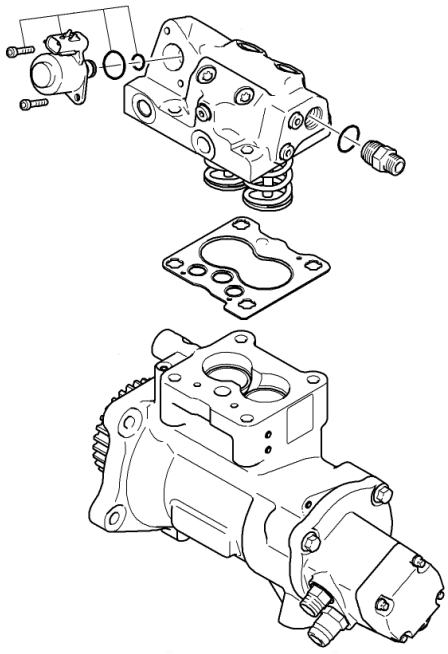

Figure 15 – Exploded view of the high pressure fuel pump (HPP) *[5]*.

The pump guarantees four strokes per crank shaft revolution, with a plunger lift of 14 *mm* per stroke. The pump pulses are clearly visible in the characteristic of its demanded torque, shown in Figure 16.

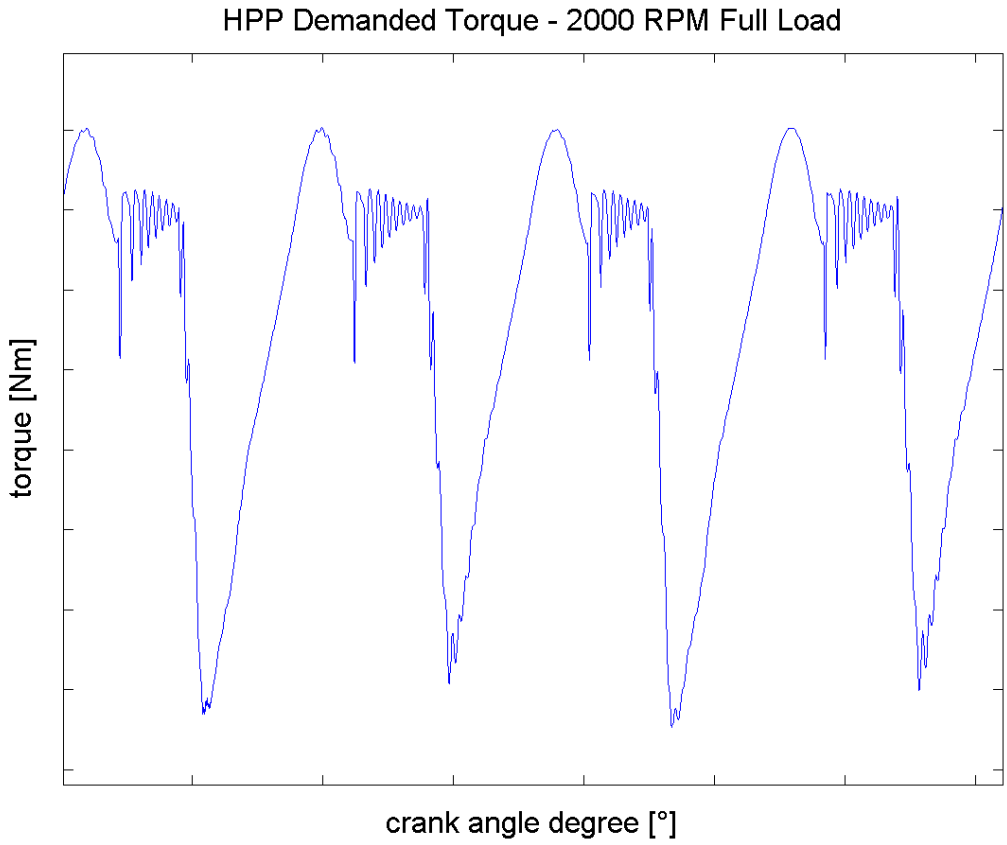

Figure 16 – Characteristic of the high pressure pump demanded torque at 2000 RPM, full load. Four peaks due to the pump strokes per crank shaft revolution are clearly visible.

The injectors tested – part number 2264458 – are characterized by 10 spray holes with a minimum nominal diameter of $0.2\ mm$. The hydraulic flow specified is $140\ kg/h$ by MFG. Method & Process STD. 77002.

The rail pressure and the current commanding the injector needle lift have been recorded. In every test, both signals have been acquired at 0.1 CAD sampling rate.

The rail pressure, in particular, has been measured through a rail pressure transducer, characterized by a maximum tolerance of $\pm 50\ bar$ within the common operating temperatures in the rail.

The current command from the ECU has been recorded by using a current clamp provided by Scania CV AB (35300128).

Engine steady and transient behaviours have been investigated. The steady operating points acquired are shown in Figure 17: Signals have been recorded for a total number of 50 complete engine cycles - 100 crank shaft revolutions - per operating point tested.

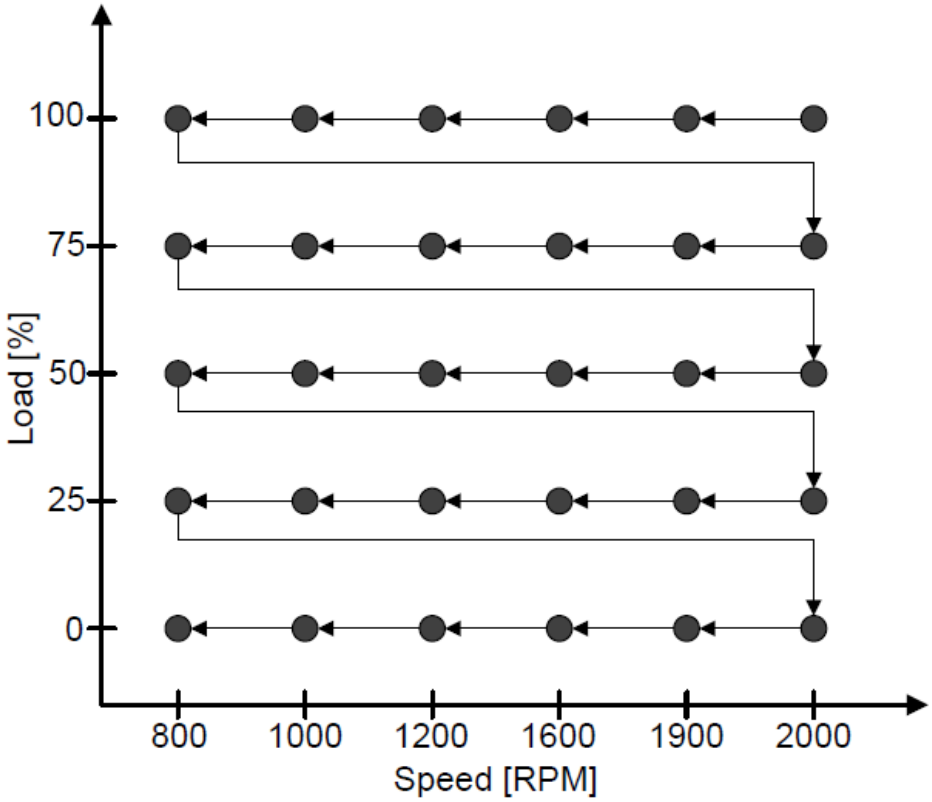

Figure 17 – Steady operating points of the D13 Scania engine tested. Signals have been acquired at 0.1 CAD sampling rate for a total number of 50 complete engine cycles (100 crank shaft revolutions) *[19]*.

The engine response to variable load and variable speed has been analysed. In particular tests have been performed for:

- Constant load, ramp in speed. These tests were performed for constant loads of 25% , 50% and 75% , the initial speed being 1200 rpm, followed by an increase of 40 rpm/s for a total time of 5 seconds.
- Constant speed, ramp in load. These tests were performed for constant speeds of 800 rpm, 1200 rpm and 1500 rpm and a load increase of 100 Nm/s for a total time of 5 seconds.

5 RESULTS: EXPERIMENTAL EVALUATION

This chapter presents a thorough analysis of the system under investigation. Results from the experimental campaigns will be employed in order to grasp the system dynamics and understand the main challenges to be faced.

5.1 Single Injection Case

In [18], the effect of a single fuel injection in terms of rail pressure oscillations has been investigated at different rail pressures and for different injected quantities, see Table 2. Tests have been conducted on the test oil ISO 4113 at a controlled rail temperature of 40°C. No pump contribution and no deflagration in the combustion chamber took place.

Table 2 – Investigation of the effects of a single fuel injection in terms of rail pressure oscillations at different rail pressures and for different injected quantities *[18]*.

Test	Engine Speed	Rail Pressure	Fuel Injected
Test 1	600 RPM	1000 bar	200 mg
Test 2	600 RPM	1000 bar	300 mg
Test 3	600 RPM	2000 bar	200 mg
Test 4	600 RPM	2000 bar	300 mg

In Figure 18, the pressure drop following the injection is reported. Note the oscillations generated by the sudden closure of the injector. An instability is propagating in the system: The water-hammer effect.

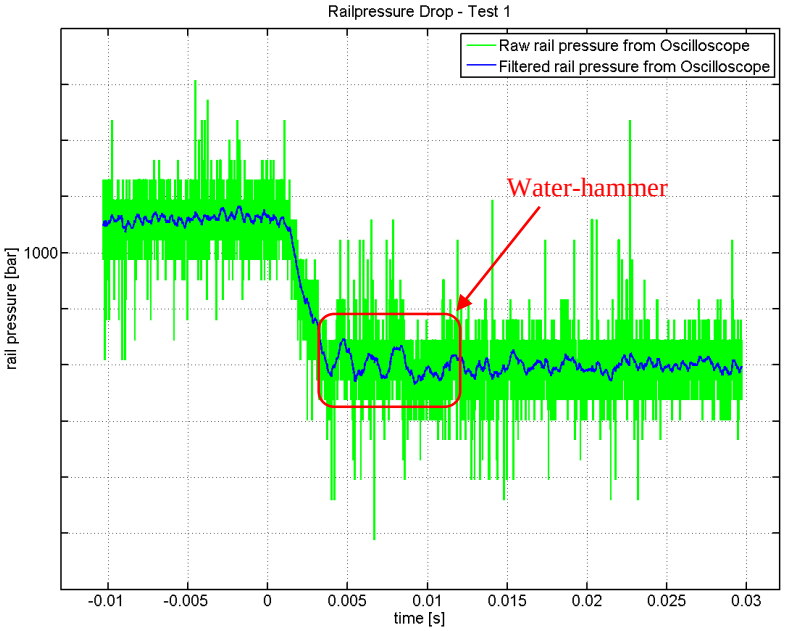

Figure 18 – Rail pressure drop in Test 1. Both raw and filtered signal from the oscilloscope are reported *[18]* , note the oscillations following the sudden closure of the injector: The water-hammer effect.

The pressure drop Δp following an injection can be predicted via Equation (54) if the amount of fuel injected (Δm_{inj}) and the total volume of the system under investigation (V_{tot}) are known [8].

$$\Delta p_{est} = -\bar{K}\frac{\Delta m_{inj}}{\bar{\rho}_{fuel} \cdot V_{tot}} \qquad (54)$$

Where $\bar{K}$ is the fuel bulk modulus and $\bar{\rho}_{fuel}$ its density. The nominal volume of the XPI system is $V_{tot} = 110\ cm^3$, including the rail, the fuel lines, the injectors, the high pressure connectors and the high pressure pump.

The results of Equation 54 are shown in Table 3. The injection process is assumed to be ideal: The actual fuel injected matches perfectly the commanded amount. The density $\bar{\rho}_{fuel}$ and the bulk modulus $\bar{K}$ are linearly interpolated from data in [18] by assuming the rail temperature constant at 40°C and the rail pressure computed as average of the pressure drop across the injection.

Table 3 – Estimation of the rail pressure drop across an injection. Equation 54 leads to larger errors for lower rail pressures: The needle mechanical response to the ECU command is slower and the amount of fuel injected might differ sensibly from the ECU commanded quantity [7].

Test	$P0_{rail}$ (bar)	Δm_{inj} (mg)	$\bar{\rho}_{fuel}$ (kg/m^3)	$\bar{K}$ (GPa)	Δp_{est} (bar)
Test 1	1012	200	837.90	2.2750	-50.28
Test 2	1012	300	837.41	2.2612	-75.42
Test 3	1994	200	878.34	3.1238	-65.57
Test 4	1998	300	877.98	3.1125	-98.04

The pressure drop estimation associated with Equation (54) is affected by tolerances over the real volume of the system, the linearization of the fuel properties and the actual amount of fuel injected. The geometrical tolerances over the volume of the high pressure fuel system, in particular, are estimated to be approximately $\pm X cm^3$, resulting in a pressure deviation of $\pm 1\ bar$.

In order to characterize the water-hammer effect observed in Figure 18, a spectral analysis of the rail pressure signal after the injector closure is required, see Figure 19.

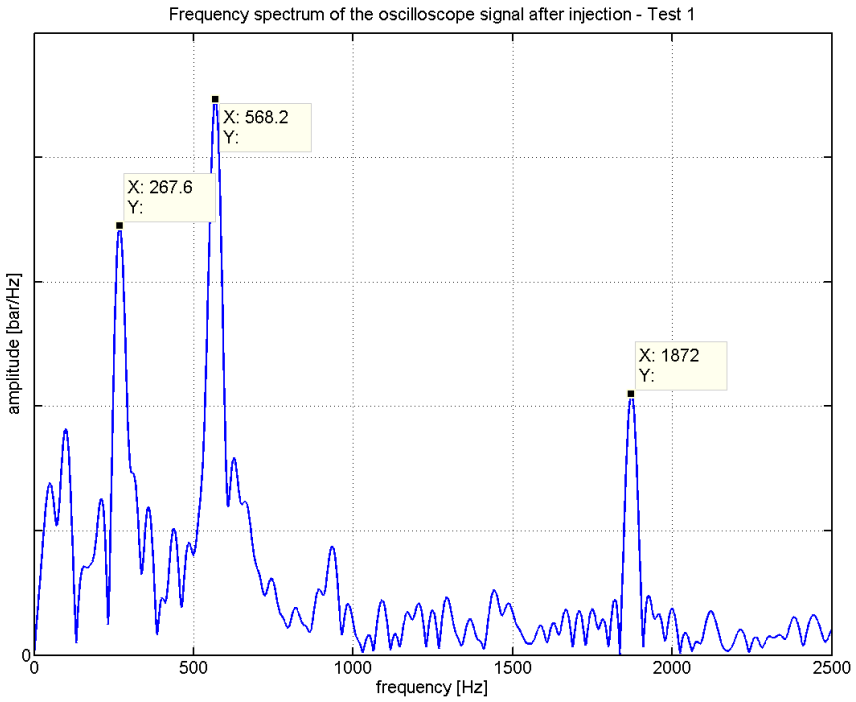

Figure 19 – Fourier transform of the rail pressure signal after the injector closure. Note the first two peaks at 267 Hz and 568 Hz generated by the propagation of the water-hammer front wave *[18]*.

Three prominent peaks in the frequency domain are found at approximately $267\ Hz$, $568\ Hz$ and $1872\ Hz$. While the peak at $1872\ Hz$ is supposed to be due to faults in the sensor employed [18], the first two peaks take their origin from the propagating wave front following the water-hammer at the injector closure. In order to support this claim, the relations for the acoustic resonance frequency in a fluid column are investigated.

The length of the 1D fluid column considered includes, starting from the injector to the pump: The high pressure connector, the injecting fuel line, the rail and the high pressure pump line for a total length of $L_{fluid} = 1.55\ m$. Different relations apply on the column resonance frequencies depending on the boundary conditions holding at the column extremes [20]. For both extremes being open or closed, i.e. respectively open injector and pump feeding the system or closed injector and no pump contribution, Equation (55) holds:

$$f_{n+1} = (2n+1)\frac{a}{4L_{fluid}} \text{ with } n = 0\,,1\,,2\,\ldots \qquad (55)$$

Where $(n+1)$ stands for the order of the harmonics, while a is the speed of sound in the mean. For a mixed boundary condition - open end close end - the frequencies of the resonance harmonics are found accordingly to Equation (56).

$$f_n = \frac{n \cdot a}{2L_{fluid}} \qquad (56)$$

Equation (55) and Equation (56) describe ideal cases. Corrective coefficients should be employed in order to obtain a higher accuracy. For further details, see [21].

The application of Equation (55) and Equation (56) to the fluid column considered should give as result the frequency peaks found in the Fourier transforms of the rail pressure signal. As Table 4 shows, however, the relative errors of the estimated resonance frequencies – first harmonics – are considerably high.

Table 4 – The application of Equation 55 and 56 on the fluid column considered leads to large error in the estimation of the system resonance frequencies.

Test	$Peak\ 1$ (Hz)	$Peak\ 2$ (Hz)	$P1_{est}$ (Hz)	$P2_{est}$ (Hz)	ε_1 %	ε_2 %
Test 1	267.64	567.42	246.58	493.32	7.9	13.1
Test 2	262.88	567.48	245.04	490.08	6.8	13.6
Test 3	316.56	657.75	289.82	579.64	8.6	11.9
Test 4	310.53	642.77	288.74	577.48	7.0	10.2

The source of this deviation lays in the design of the high pressure connector, provided with an internal mechanical filter as Figure 20 shows.

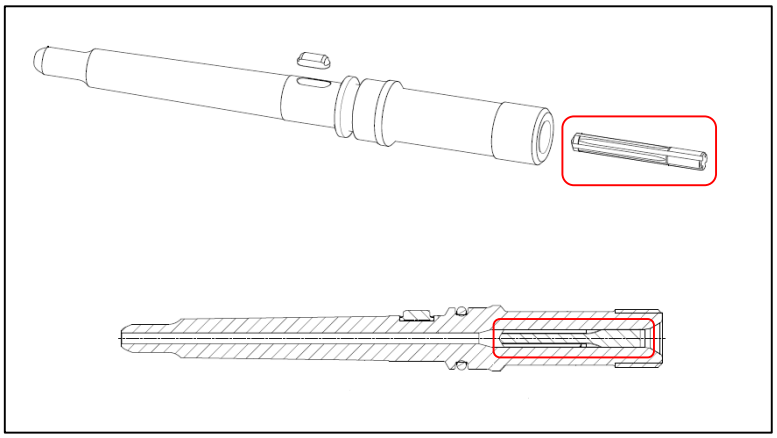

Figure 20 – HPC. The high pressure connector design includes a mechanical filter preventing the water-hammer perturbation from reaching the injector. HPC Part number - 1832724.

The HPC filter prevents the front wave from propagating through the high pressure connector till the injector. The actual fluid column to be considered for the computation of the resonance frequencies, therefore, does not account for the HPC segment, resulting in a shorter length $L_{fluid} = 1.405\ m$. The results reported in Table 5 show a significant reduction in the relative error associated with the estimation.

Table 5 – For a fluid column of length $L_{fluid} = 1.405\ m$, satisfying estimation of the frequency peaks in Figure 19 can be achieved.

Test	$Peak\ 1$ (Hz)	$Peak\ 2$ (Hz)	$P1_{est}$ (Hz)	$P2_{est}$ (Hz)	ε_1 %	ε_2 %
Test 1	267.64	567.42	271.77	543.50	1.5	4.2
Test 2	262.88	567.48	270.06	540.12	2.7	4.8
Test 3	316.56	657.75	319.41	638.83	0.9	2.9
Test 4	310.53	642.77	318.22	636.44	2.5	1

It can be concluded that the propagation of the water-hammer front wave observed through the standard rail pressure sensor does not affect the fuel trapped in the high pressure connector. This water-hammer instability propagates in the system but is prevented from reaching the injector. The flow instabilities at the injector side could not be observed and should be further investigated.

The effect of the water-hammer instability on the pressure measurement will be discussed in further details in the next sections.

5.2 Engine Steady Operating Points

In the experimental campaign conducted by the author in collaboration with Maryam Shoe and the CLCC group, the rail pressure dynamics has been investigated at several engine operating points. Figure 21 shows the signal recorded for an engine speed of 1200 RPM, full load.

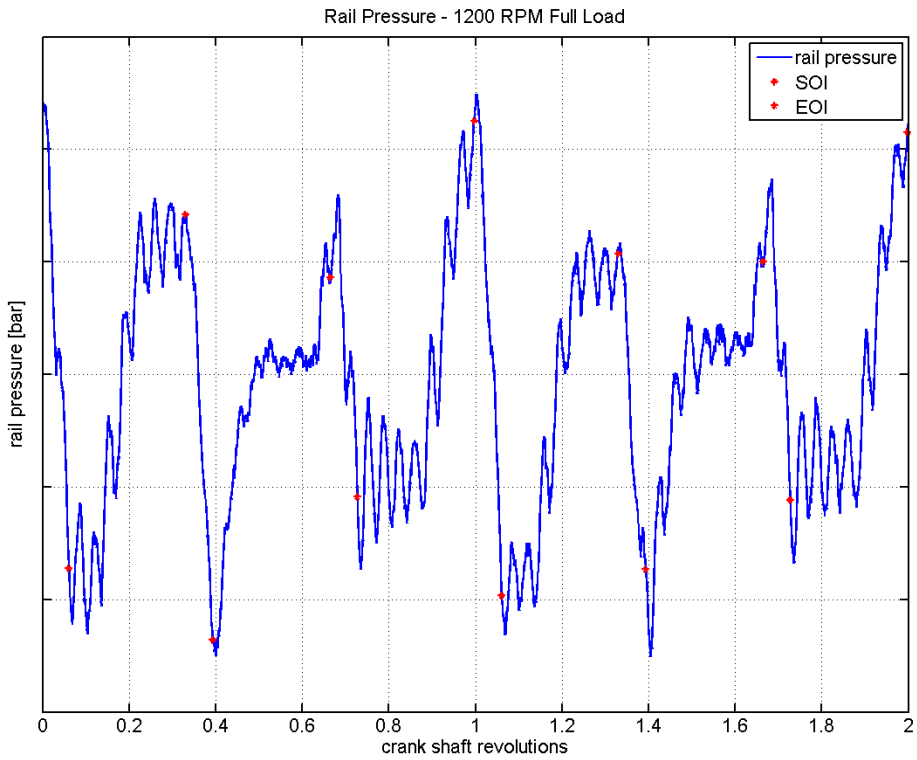

Figure 21 – Rail pressure dynamics at 1200 RPM, full load. As expected, a pressure drop follows the start of injection (SOI), while a water-hammer perturbation ensues the injector closure - end of injection (EOI).

As found for the single injection case, the water-hammer instability plays a major role in the rail dynamics, Figure 22.

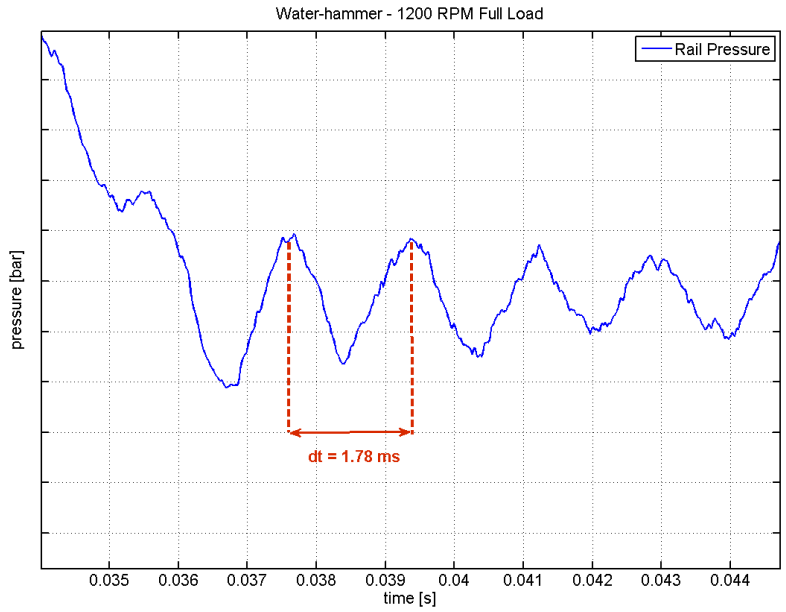

Figure 22 – Zoom on the water-hammer instability following the sudden closure of the injector. The main frequency associated with the wave propagation is in this particular case approximately $\sim 560\ Hz$.

In order to fully characterize the case under study, an investigation in the frequency domain is required. In Figure 23 the Fast Fourier Transform (FFT) of the pressure signal acquired is shown: Peaks at the injection harmonics and at the HPP strokes harmonics are clearly visible. The resonance frequencies of the fluid column involved in the water-hammer propagation are found at approximately $\sim 280\ Hz$ and $\sim 550\ Hz$.

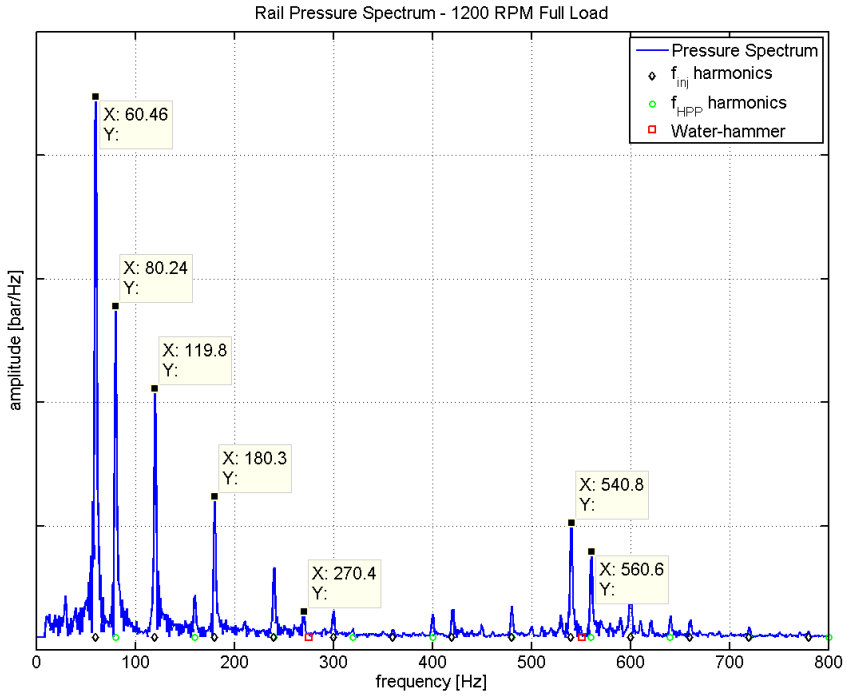

Figure 23 – Spectrum of the rail pressure signal, 1200 RPM full load. Peaks at the injection harmonics and at the HPP strokes harmonics are clearly visible. The resonance frequencies of the fluid column involved in the water-hammer propagation are found at approximately ~280 Hz and ~550 Hz.

At the highest resonance frequency, in particular, a superposition between the injection harmonics, the HPP harmonics and the water-hammer concurs in an over-excitation of the system. As Figure 24 shows, the excitation of the system resonance frequency is higher for higher engine loads, i.e. for higher amount of fuel injected, Figure 25. For high fuel injection rates, the sudden closure of the injector causes an abrupt stop of the flow, followed by a strong water-hammer perturbation [8].

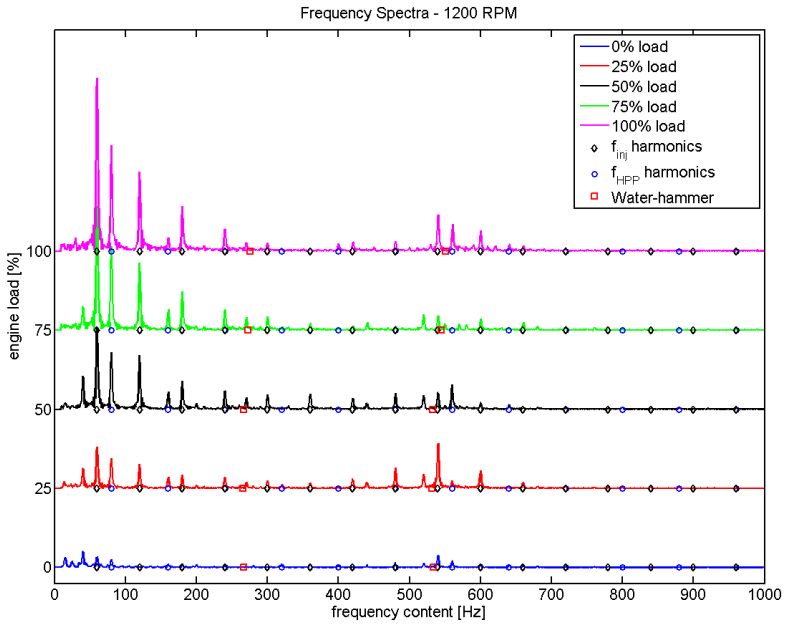

Figure 24 – Waterfall diagram: rail pressure spectra for different loads at constant 1200 RPM engine speed. The superposition between the injection harmonics, the HPP harmonics and the water-hammer concurs in an over-excitation of the system at the highest fluid column resonance frequency. At low loads, the fuel injection rate is lower and therefore a sudden closure of the injector results in a weaker water-hammer effect.

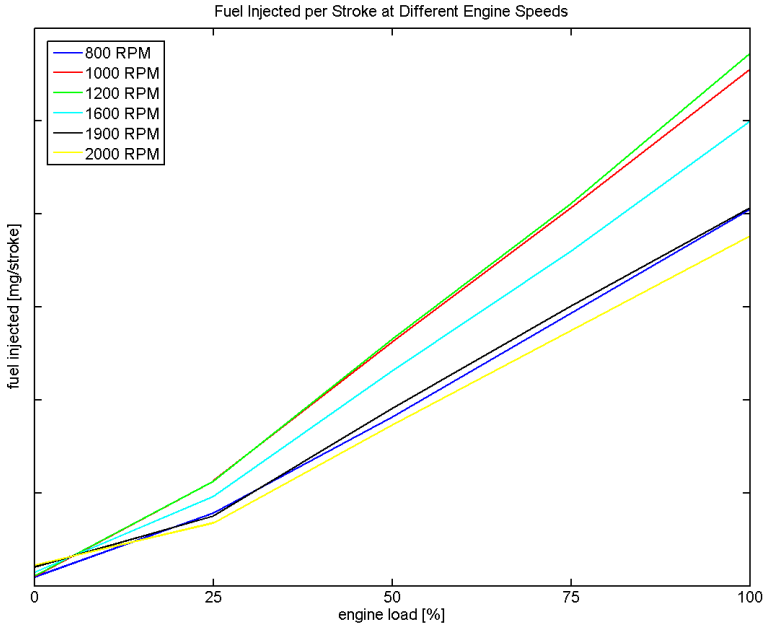

Figure 25 – The amount of fuel injected per stroke increases almost linearly with the engine load at every engine speed.

For a particular fuel, the system resonance frequency mainly depends on the rail pressure and temperature. These affect the speed of sound in the mean and therefore the propagation of the water-hammer instability, see Equation (55) and Equation (56). As Figure 26 shows, at higher rail pressures, a higher speed of sound results in higher resonance frequencies. No direct influence of the engine speed is found: The order of the harmonics excited depends only on the system resonance frequency.

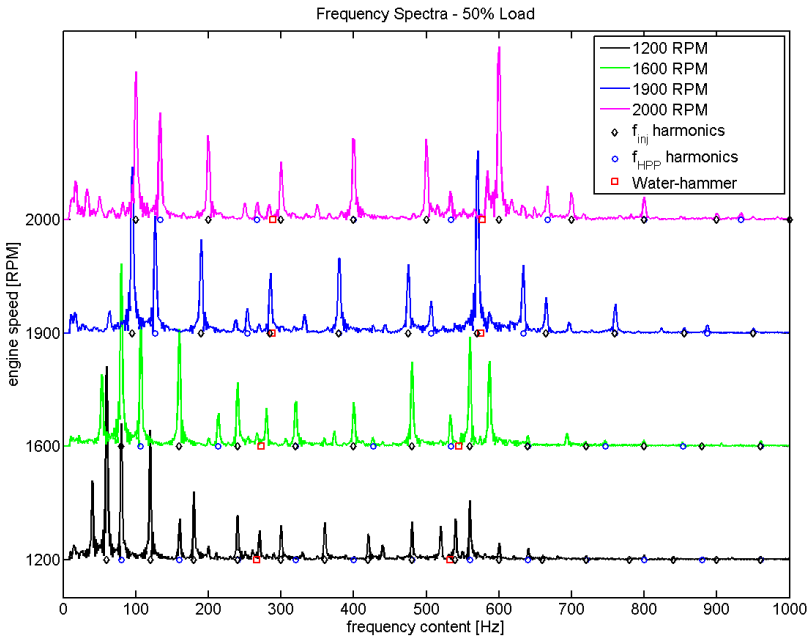

Figure 26 – Waterfall diagram: rail pressure spectra for different engine speeds at 50% constant load. At higher rail pressures, a higher speed of sound results in higher resonance frequencies. No direct influence of the engine speed is found: The order of the harmonics excited depends only on the system resonance frequency.

6 RESULTS: MODEL EVALUATION

This chapter presents the results from the model developed. Several limits have been found and suggestions for further improvements are given.

Figure 27 shows a comparison between experimental data – blue line – and model results – red dashed line – for an engine speed of 2000 RPM, full load. Clearly, the model shows major faults in phase synchronization and it is characterized by relevant overshoots in the estimation of pressure peaks.

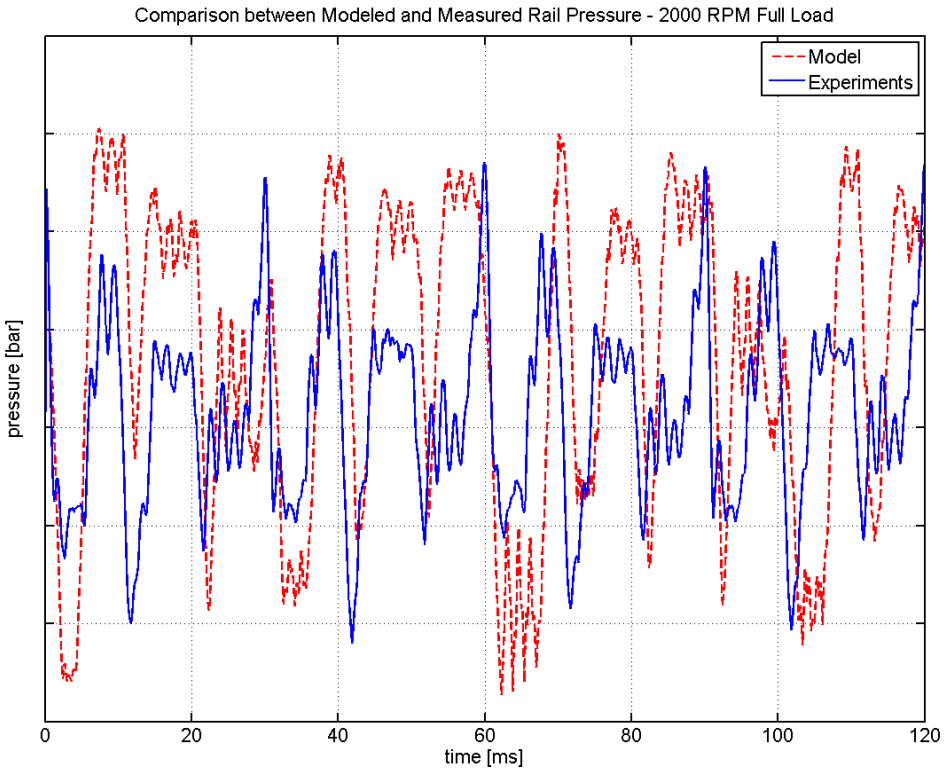

Figure 27 – 2000 RPM full load: the model shows major faults in phase synchronization and it is characterized by relevant overshoots in the estimation of pressure peaks.

The proposed model, however, is capable of detecting the expected frequency contents of the phenomenon investigated, indicating a correct interpretation of the physical phenomenon under analysis. The main frequency contents due to injections, pump strokes harmonics and water-hammer are reported in Figure 28.

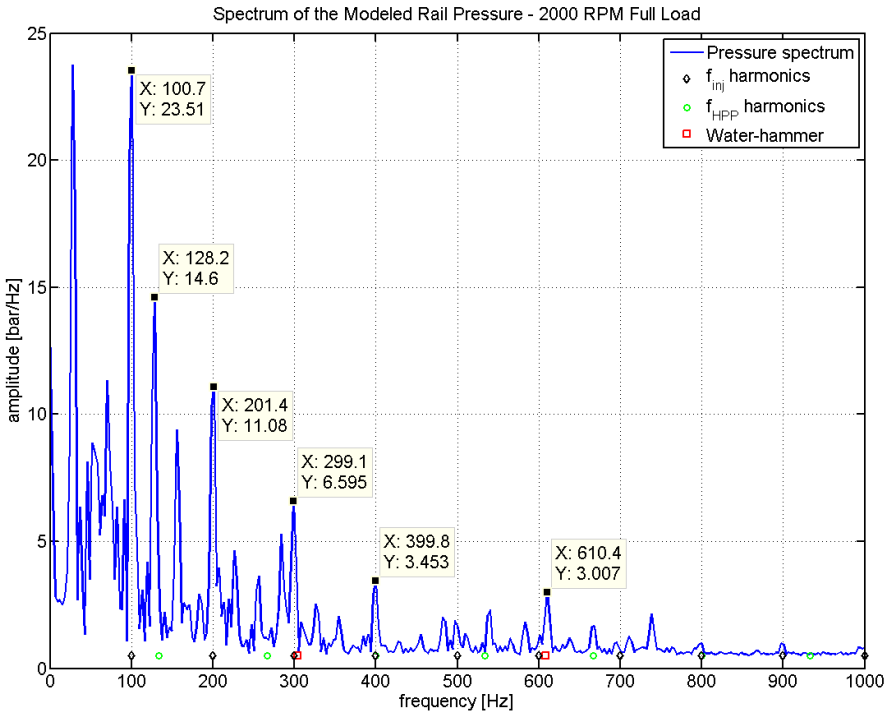

Figure 28 – Model pressure spectrum: The proposed model is capable of detecting the expected frequency contents of the phenomenon investigated, indicating a correct interpretation of the physical phenomenon under analysis. The main frequency contents due to injections, pump strokes harmonics and water-hammer are shown.

The mean estimation offsets tend generally to increase with higher engine loads up to a maximum error of approximately 50 *bar*, Figure 29.

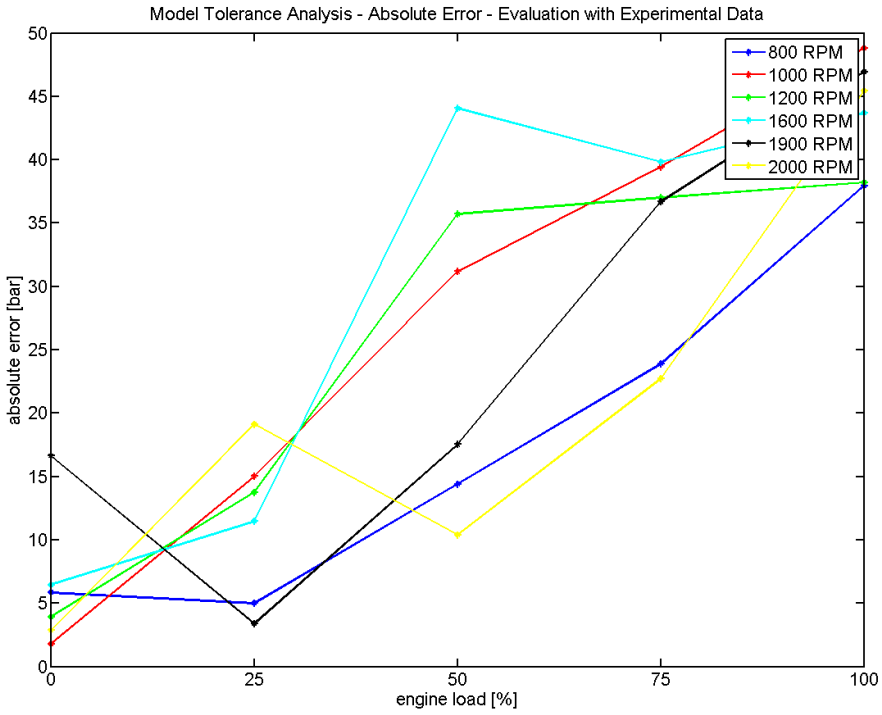

Figure 29 – Model evaluation with experimental data: The estimation offsets tend generally to increase with higher engine loads up to a maximum error of approximately 50 *bar*.

Each simulation has been conducted with a time step $dt = 2\ \mu s$. Figure 30 shows the effect of the grid resolution over the obtained results. A suitable time step should guarantee the independence of the results achieved from the grid resolution. As Figure 30 shows, however, the chosen time step does not fulfil the sought requirement. Simulations have been conducted in the Matlab® environment, where no smaller time step was allowed. In order to improve the model performances, a more efficient numerical scheme should be implemented. Suitable choices have been identified in the SIMPLE and PISO algorithm [22].

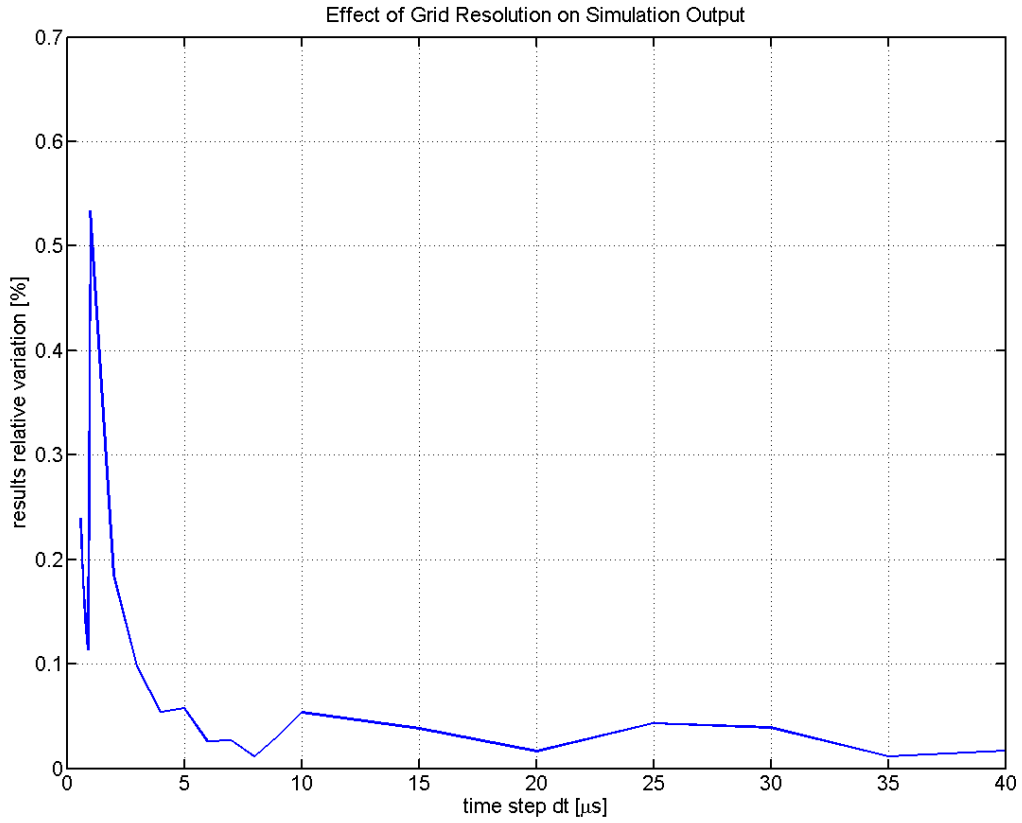

Figure 30 – Effects of the grid resolution on the model results: A suitable time step should guarantee the independence of the results achieved from the grid resolution. The chosen time step, however, does not fulfil the sought requirement. In order to improve the model performances, a more efficient numerical scheme should be implemented. Suitable choices have been identified in the SIMPLE and PISO algorithm *[22]*.

In Chapter 2 and Chapter 3, the assumptions holding beneath the developed model have been listed. Figure 31 shows the effects that geometrical tolerances on the system volume ($\pm X\ cm^3$), temperature variations ($\pm\ 20°C$) and the use of a different fuel (German diesel) would have on the model results. While geometrical tolerance do not have a major impact, temperature variations in the system have a deep influence on the system characterization. The assumption of an isothermal system, therefore, is not applicable and temperature gradients should be taken into account in future attempts to model the high pressure fuel system. As Figure 31 shows, the model is univocally suitable for a particular kind of fuel.

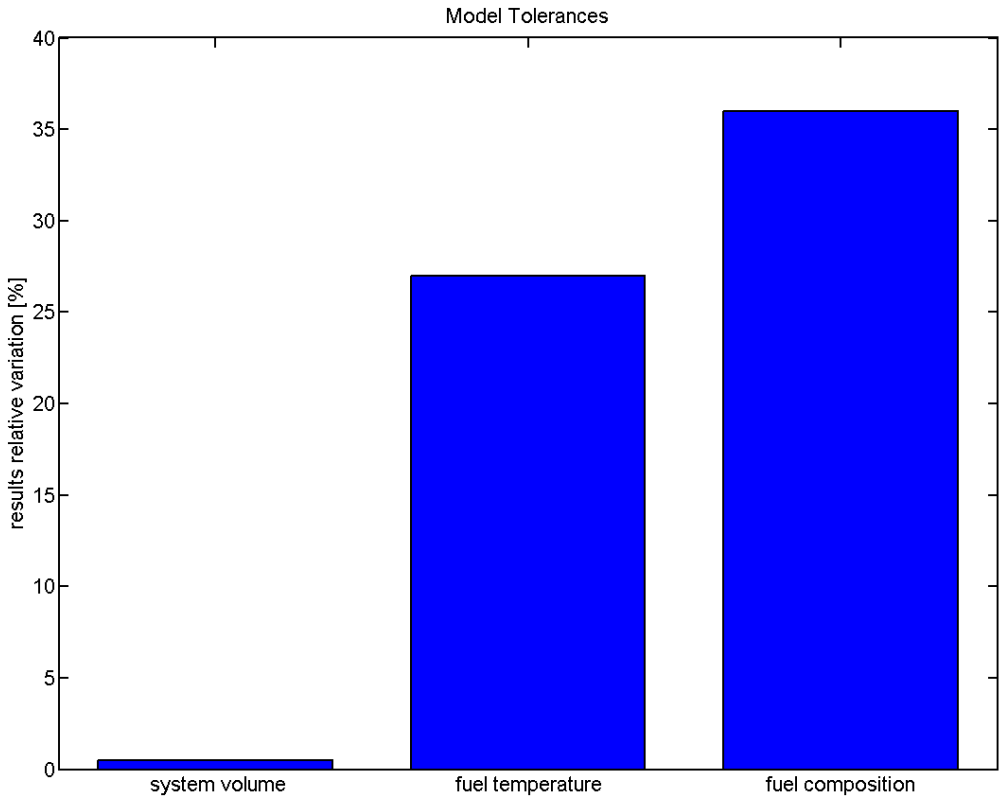

Figure 31 - Effects that geometrical tolerances on the system volume ($\pm Xcm^3$) temperature variations (± 20°C) and the use of a different fuel (German diesel) would have on the model results. While geometrical tolerance do not have a major impact, temperature variations in the system have a deep influence on the system characterization. Moreover, the model is univocally suitable for a particular kind of fuel.

7 RESULTS: SAMPLING THE PRESSURE

This chapter gives a deep evaluation of the current sampling technique implemented today at Scania CV AB in order to measure the rail pressure. A new sampling method is also proposed for engine steady operations.

7.1 Evaluation of the Current Sampling Technique

As shown in Section 1.4, two parameters concur in determining the injection ontime: the amount of fuel commanded by the ECU and the rail pressure available in the software. Due to the rail pressure fast transients, the available pressure can vary significantly from the actual pressure at the injector: The given injection ontime combined with the actual rail pressure results in a different amount of fuel injected from what the ECU requested. This section aims at a quantitative and detailed evaluation of the consequences following the current measurement technique implemented today by Scania CV AB.

The current sampling technique aims at estimating the average rail pressure across each injection and therefore the absolute estimation error of the current sampling technique should be computed with respect to the pressure found as:

$$\bar{P}_{inj} = \frac{P_{SOI}+P_{EOI}}{2} \qquad (57)$$

In order to obtain an as accurate as possible reference mean pressure across the injection, the start and end of injections should be known with negligible uncertainties. However, the ECU estimation for the SOI and EOI can be slightly inaccurate and, as Figure 32 shows, this offset leads to important tolerances in the reference pressure expressed in Equation (57).

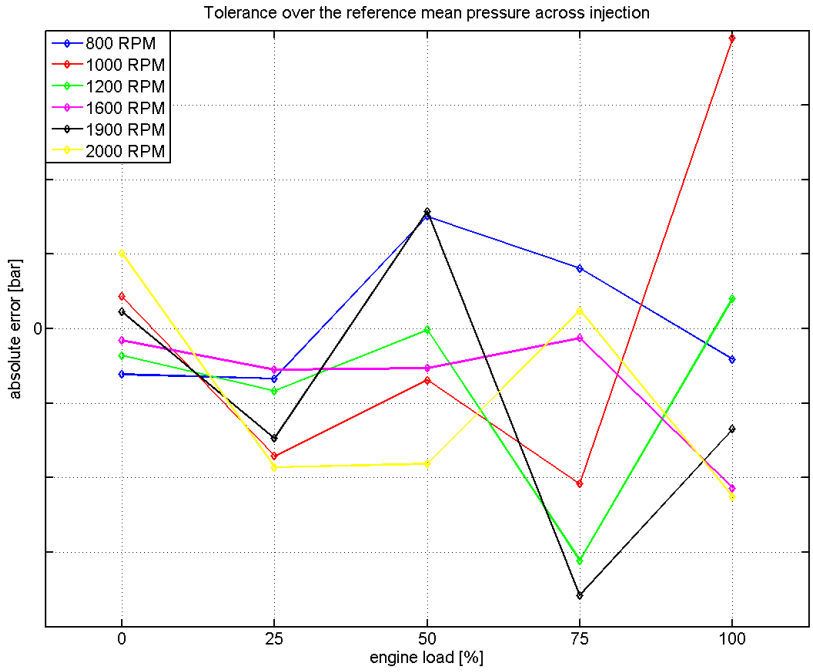

Figure 32 – Tolerances over the reference pressure adopted for the following analysis. These offsets might deeply affect results and conclusions of the following analysis, hence they cannot be accepted as negligible and further investigation is required for a full validation of the results presented.

The pressure sensor tolerance also plays a relevant role in the estimation of $\bar{P}_{inj}$, with a maximum tolerance of $\pm 50\ bar$. These tolerances over the reference pressure can deeply affect results and conclusions of the following analysis, hence they cannot be accepted as negligible. In order to fully validate the results presented later in this section, the following analysis should be repeated for several sensors and with a better accuracy over the actual start and end of injection.

In Figure 33, for an engine speed of 2000 RPM, full load, the measured rail pressure – blue line – is shown together with the mean rail pressure across each injection – green line – and the ECU estimation – red line. The inability of the ECU in catching the pressure fast transients is clearly visible.

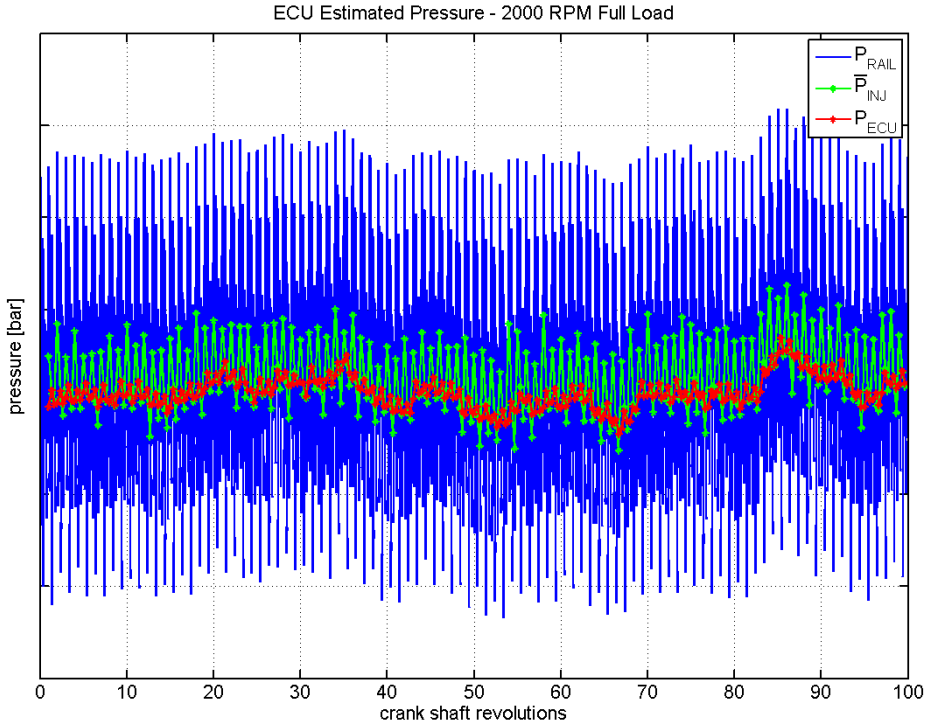

Figure 33 - 2000 RPM, full load: The measured rail pressure – blue line – is shown together with the mean rail pressure across each injection – green line – and the ECU estimation – red line. The inability of the ECU in catching the pressure fast transients is clearly visible.

Five possible sources of error have been identified:

1. Pressure sensor tolerances.

2. Offsets in the estimation of the actual start and end of injection.

3. The age of data: The estimation of the mean pressure across the injection is not always based on the newest samples acquired.

4. The water-hammer generated instability: The oscillations following the injector closure affect the measurement.

5. The HPP syncing to the crank shaft: A pump stroke taking place during an injection deeply affects its average rail pressure.

Figure 34 shows, for 2000 RPM full load, the average rail pressure across each injection (*pressure to be estimated*), and the ECU estimations according to the age of the data employed. In particular *pressure estimation 1* is computed on the newest samples, while *pressure estimation 2* is computed on the previous ones available. The estimated SOI and EOI are reported also.

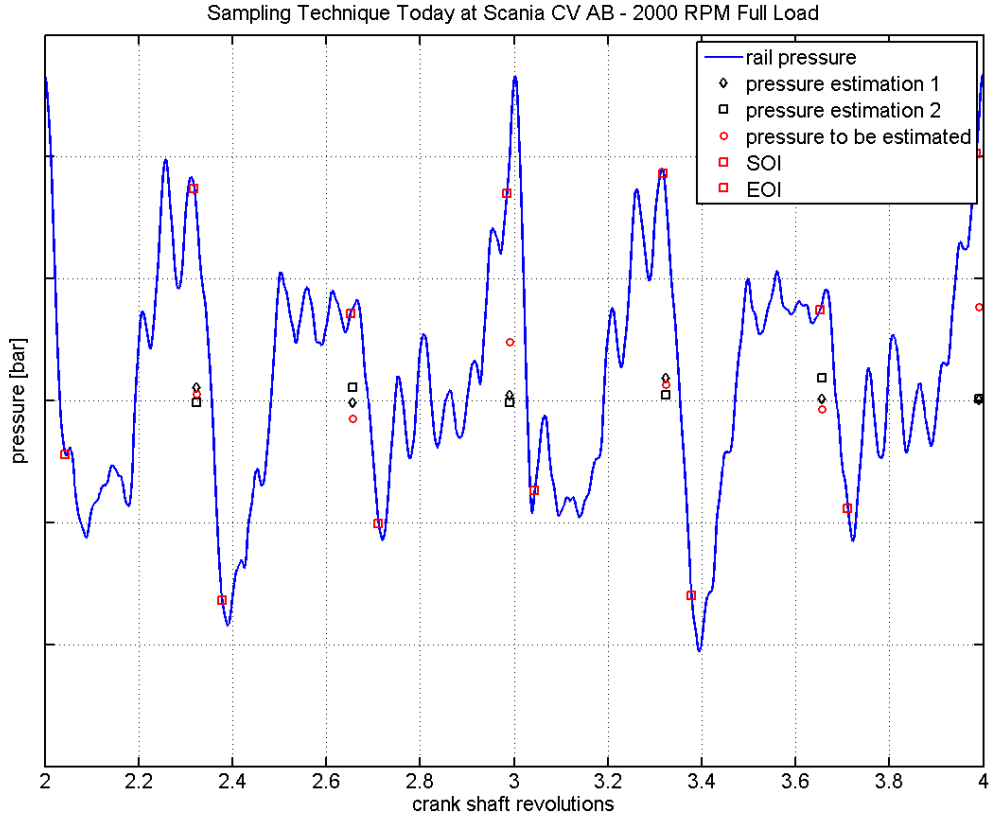

Figure 34 – 2000 RPM full load: The average rail pressure across each injection is shown (*pressure to be estimated*), and the ECU estimations according to the age of the data employed. In particular *pressure estimation 1* is computed on the newest samples, while *pressure estimation 2* is computed on the previous ones. The estimated SOI and EOI are reported also.

As Figure 34 suggests, the age of data does not seem to have a net influence over the estimation offsets. In order to support this claim, an analysis of the absolute errors for the analysed operating points has been carried out. Figure 35 shows, for every point tested, the mean absolute error in the ECU estimation with respect to the average rail pressure calculated via Equation (57). In several cases, it can be seen that the availability of the newest pressure samples (blue symbols) does not correspond to a better accuracy, therefore the age of the data employed by the ECU cannot be the main responsible for the estimation offset alone. Note that the error tends to increase with the engine load. No influence is found of the engine speed over the error, see Appendix D.

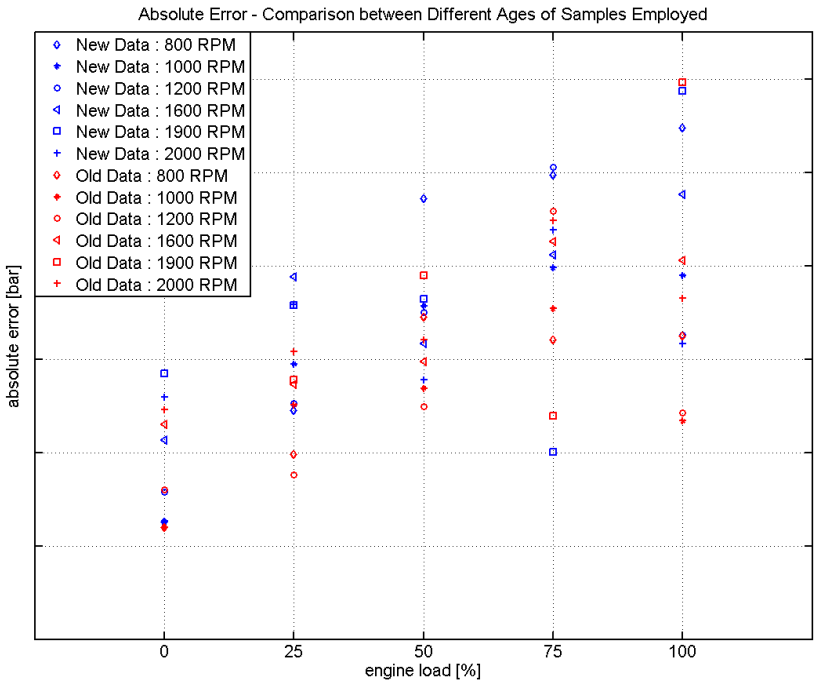

Figure 35 - For every point tested, the mean absolute error in the ECU rail pressure estimation. In several cases, it can be seen that the availability of the newest pressure samples (condition I) does not correspond to a better accuracy, therefore the age of data employed by the ECU can not the main responsible for the estimation offset alone.

Figure 36 shows the standard deviation of the mean estimation error in each operating point tested: It is significantly high in general, indicating a high dispersion in the absolute error.

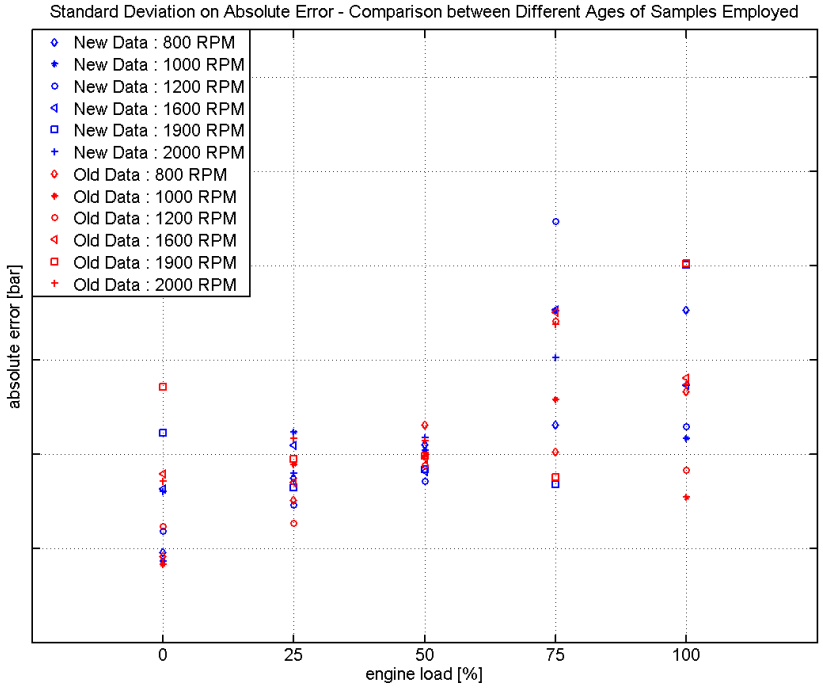

Figure 36 - standard deviation of the mean estimation error in each operating point tested: It is significantly high in general, indicating a high dispersion in the absolute error.

A second possible source of error has been identified in the water-hammer instability propagating in the system. Even though the fuel flow at the injector is not affected by such phenomenon – Section 5.1 – the pressure signal recorded accounts for such oscillations. As Figure 34 suggests, the water-hammer causes a wide spread of the samples collected across each injection. Figure 37 shows the effect of the samples spread (horizontal axis) with respect to the estimation absolute error (vertical axis). The dispersion is expressed as the standard deviation of the samples cluster around its mean value. No significant relation between samples dispersion and error is found.

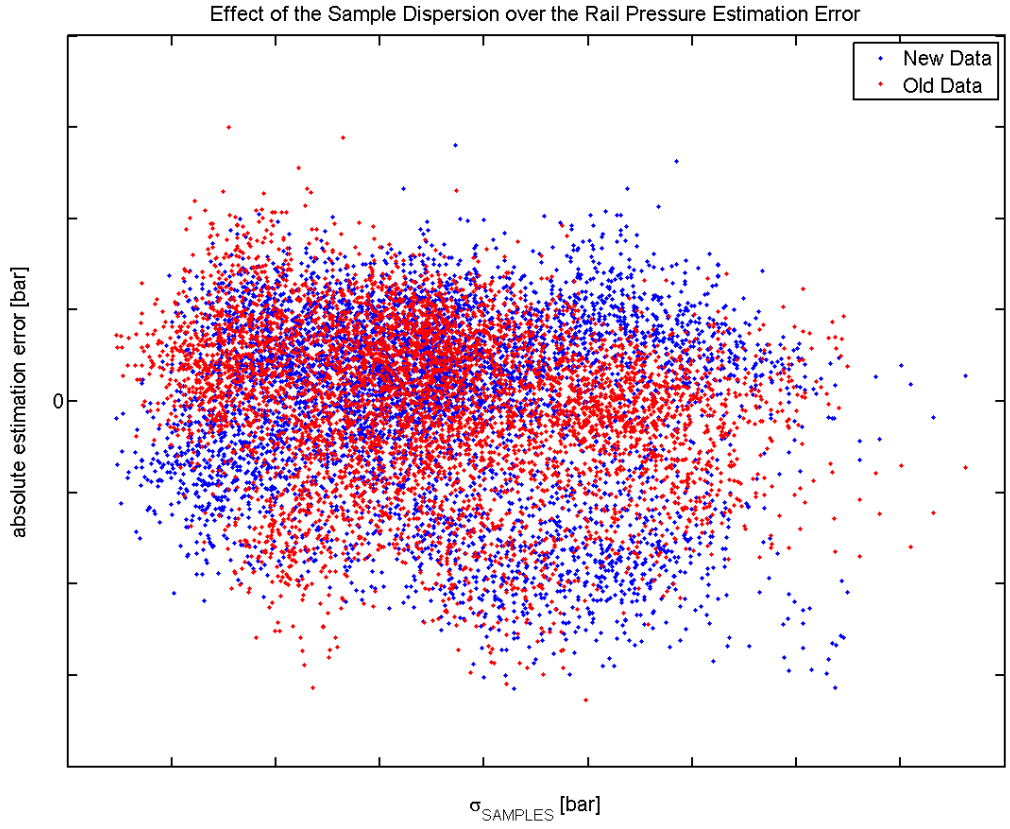

Figure 37 – Effect of the samples spread (horizontal axis) with respect to the estimation absolute error (vertical axis). No significant relation between samples dispersion and error is found.

The phase shift between the high pressure pump and the crank shaft deeply affects the rail pressure characteristic signature. As mentioned earlier, per crank shaft revolution, the HPP guarantees four strokes while three injections take place. The superposition of the two signals generates a new periodic function with one crank shaft revolution period, as Figure 34 intuitively suggests. As an example, Figure 38 shows the function resulting from the superposition of the following sine waves:

$$\begin{cases} y = \sin 3x \\ y = \sin 4x \end{cases} \qquad (58)$$

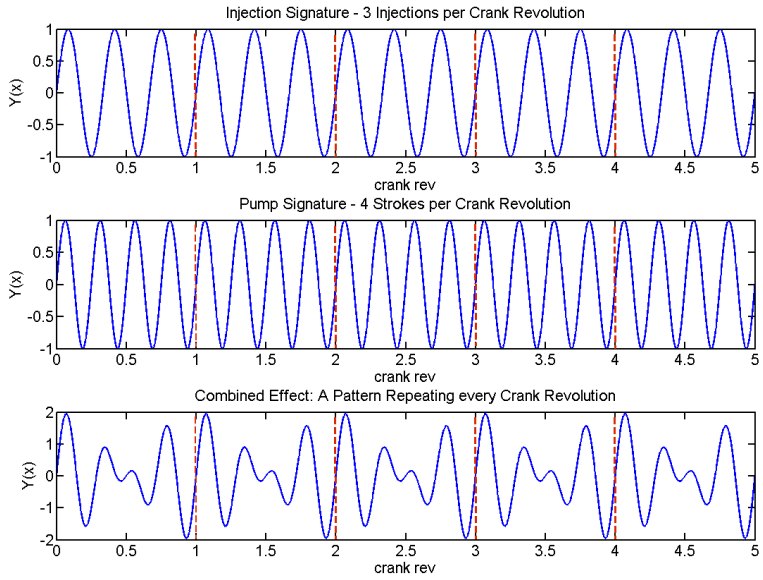

Figure 38 – Per crank shaft revolution, the injection frequency is source for three pulses, while the HPP guarantees four strokes. The superposition of the two signals generates a periodic function with one crank shaft revolution period.

The autocorrelation of a test case – 2000 RPM full load – has been analysed in order to understand how self-similar the signal is if phase shifted in the crank angle degree domain. Figure 39 shows that for the steady operating point tested, the pressure signature analysed displays a high degree of similarity for multiple phase shifts of one crank shaft revolution, as expected. It is particular interesting to note that the degree of self-similarity is higher after a delay of two revolutions: besides the periodicity of the function resulting from the superposition of injections and HPP strokes, the same injectors are involved in the injection process every two crank shaft revolutions.

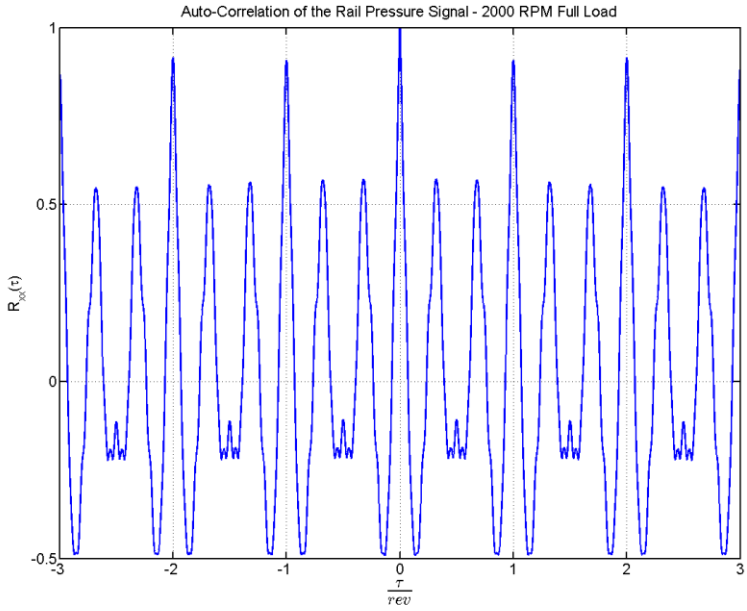

Figure 39 - The pressure signature analysed displays a high degree of similarity for multiple phase shifts of one crank shaft revolution, as expected. It is particular interesting to note that the degree of self-similarity is higher after a delay of two revolutions: besides the periodicity of the function resulting from the superposition of injections and HPP strokes, the same injectors are involved in the injection process.

In order to assess the general validity of these findings, the mean autocorrelation function of a population of five pressure signals, each recorded for a duration of ten engine cycles, has been computed for each of the other operating points acquired. The mean values found after one crank revolution delay are displayed in Figure 40. The self-similarity of the pressure signature acquired tends to increase with higher engine loads, while it appears approximately constant with the engine speed, see Appendix E. A poor self-similarity characterizes the combination of low loads and low engine speeds.

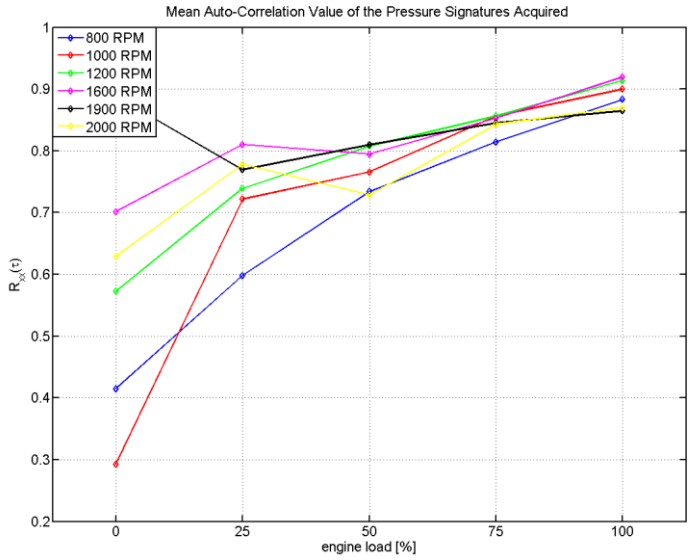

Figure 40 - Mean autocorrelation value after one crank revolution delay for every operating point tested. The self-similarity of the pressure signature acquired tends to increase with higher engine loads. A poor self-similarity characterizes low loads and low engine speeds.

Figure 41 shows the standard deviations of the results shown in Figure 40. The dispersion of the mean autocorrelation tends to decrease for higher engine load, while it results considerably high for an unloaded engine condition.

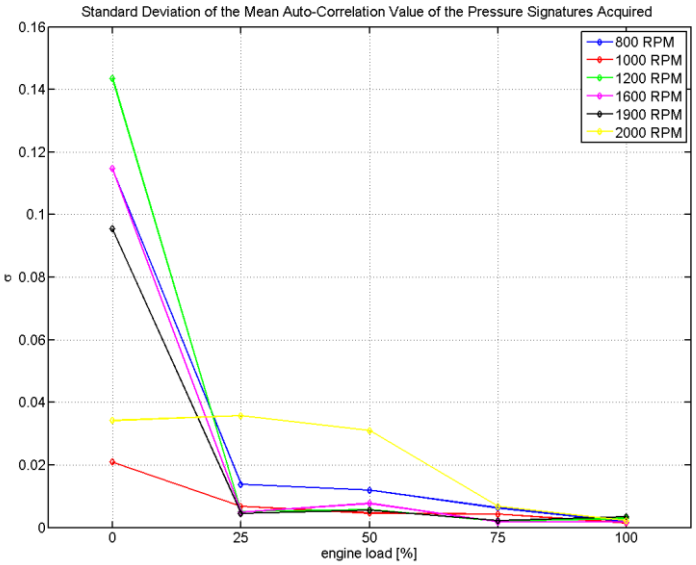

Figure 41 – Standard deviation of the mean autocorrelation value of the pressure signals acquired. The dispersion tends to decrease for higher engine load, while it results considerably high for an unloaded engine condition.

Different couplings between the high pressure pump and the crank shaft have a great impact over the resulting pressure signature. The phase shift between them, however, does not affect the periodicity of the signal resulting from the superposition of injections and HPP strokes, which has been found to be of one crank shaft revolution.

For a steady operating point, therefore, the rail pressure behaviour tends to repeat itself, within a certain degree of accuracy, every crank shaft revolution.

7.2 Proposed Sampling Technique

A new measurement technique, potentially capable of reducing the error in the rail pressure estimation, is proposed for steady engine operations. The details of the suggested technique are not given due to a confidentiality agreement between Scania CV AB and the author.

Figure 42 shows, for 2000 RPM full load, the average rail pressure across each injection (*pressure to be estimated*), and the ECU estimations via the current measurement technique and via the proposed new method. The estimated SOI and EOI are reported also. The following analysis is affected by the same tolerances on the pressure sensor and on the SOI and EOI estimations analysed in the previous section.

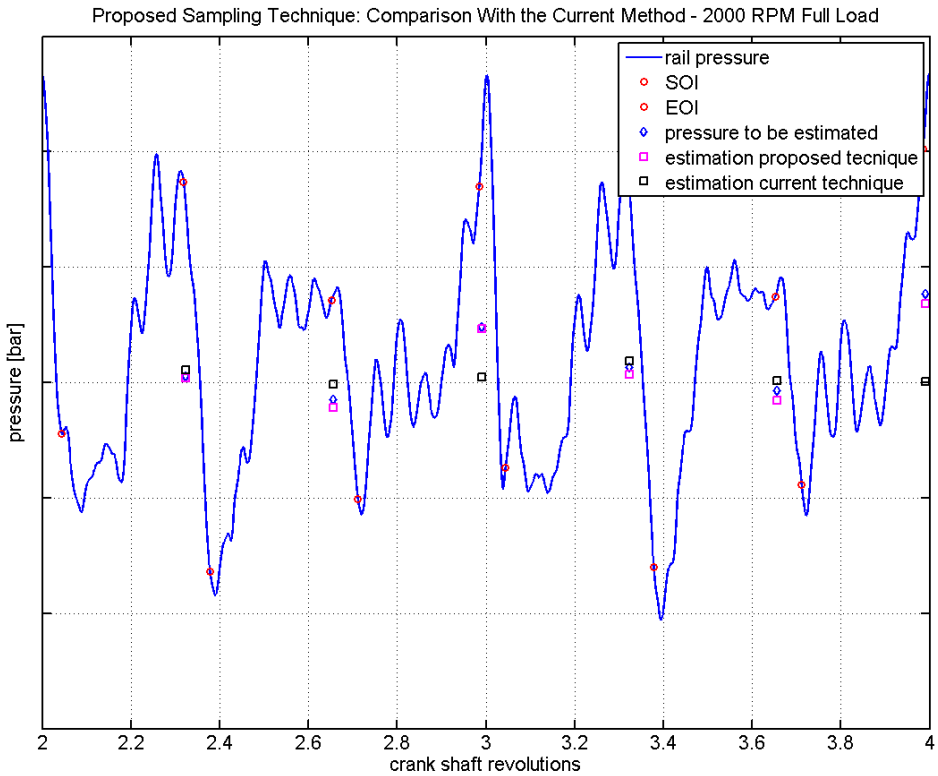

Figure 42 – 2000 RPM full load: The average rail pressure across each injection (*pressure to be estimated*) is shown together with the ECU estimations via the current measurement technique and via the proposed new method. The estimated SOI and EOI are reported also.

As Figure 42 intuitively suggests, the proposed measurement technique shows better performances. In Figure 43, in particular, the estimation errors associated with the two methods are reported. Evidence of the superior accuracy of the proposed technique for the test case analysed is given.

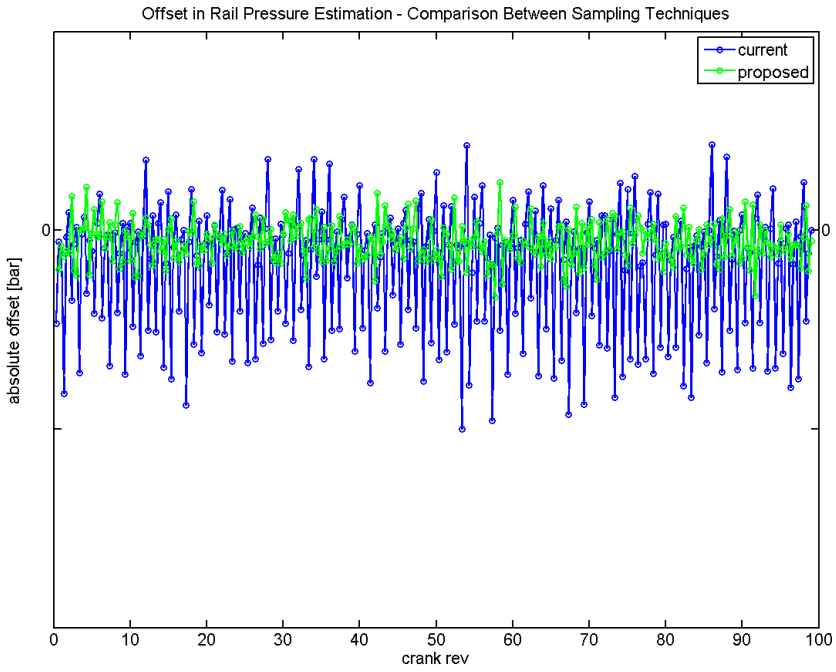

Figure 43 – 2000 RPM full load: Comparison between sampling techniques in terms of estimations errors. Evidence of the superior accuracy of the proposed technique for the test case analysed is given.

In order to assess the general validity of the proposed sampling technique, the same analysis has been carried out for all the operating points acquired. Figure 44 shows the mean offset error of both methods at each engine condition tested. The proposed method – red symbols – generally shows a better accuracy.

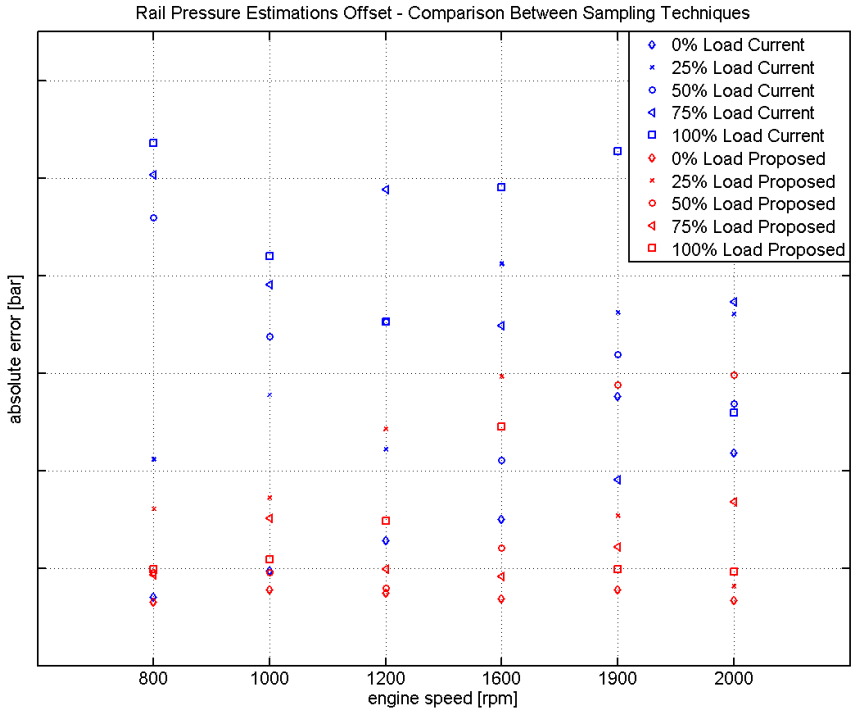

Figure 44 – Estimation offsets: The mean errors of the sampling techniques tested are shown at each engine operating point acquired. The proposed method – red symbols – generally shows a better accuracy.

Figure 45 shows the standard deviation of the mean errors reported in Figure 44: The dispersion associated with the proposed sampling – red symbols – is approximately constant along all the operating points tested, indicating a high predictability of the method performances.

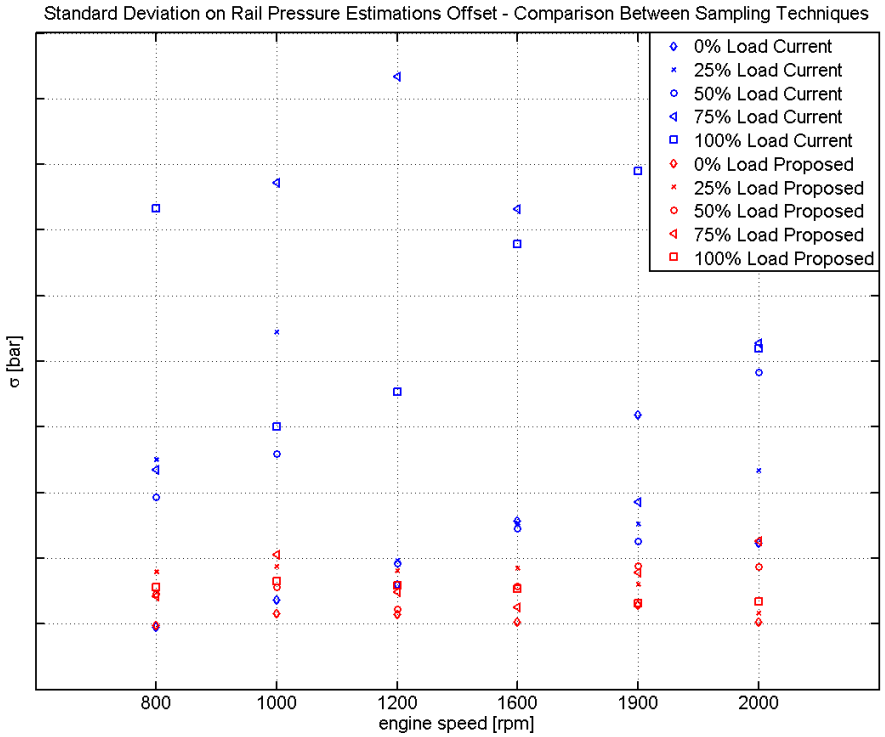

Figure 45 – Standard deviations of the mean estimation offsets: The dispersion associated with the proposed sampling – red symbols – is approximately constant along all the operating points tested, indicating a high predictability of the method performances.

As discussed in Section 1.4, the injection ontimes are experimentally calibrated offline upon the mean rail pressure and the ECU fuel request. The determined values should guarantee, within a certain degree of accuracy, the injection of the amount of fuel commanded.

During real operations, however, the mean rail pressure across an injection is not available and therefore an estimation is required. An offset in the pressure estimation results in an inaccurate selection of the injection ontime and in a poorly controlled amount of fuel injected.

In order to determine the deviation from the amount of fuel commanded, the same experimental tables for the injection ontime have been employed: Given as inputs the *measured* rail pressure and the injection ontime determined upon the *estimated* rail pressure, the actual amount of fuel injected is given as output.

Figure 46 shows, for 2000 RPM full load, the deviation from the amount of fuel commanded related to the current and proposed measurement techniques of the rail pressure.

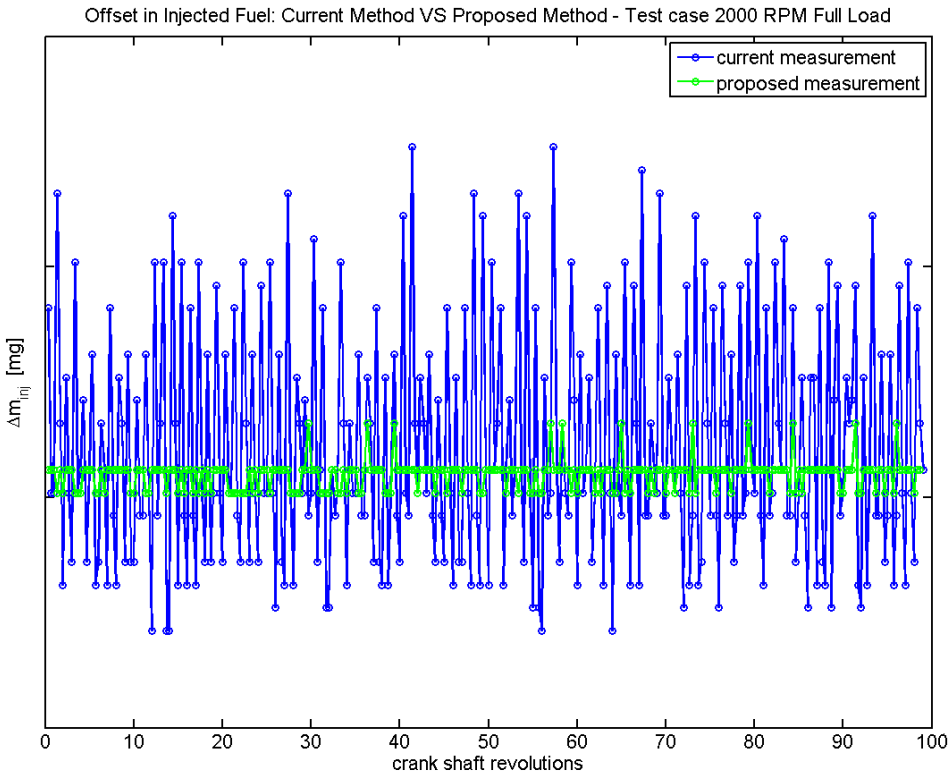

Figure 46 – 2000 RPM full load: Comparison between current and proposed measurement techniques in terms of absolute and relative error between actual fuel injected and ECU request. The proposed sampling technique guarantees a better control over the amount of fuel injected and a noise reduction.

Clearly, the proposed sampling technique guarantees a better control over the amount of fuel injected. Noise is decreased and the consequences of this potential reduction on the engine torque signature should be further investigated.

The mean deviation from the commanded amount of fuel at each of the engine operating points tested is reported in Figure 47. The superior accuracy of the proposed method – red symbols – is evident.

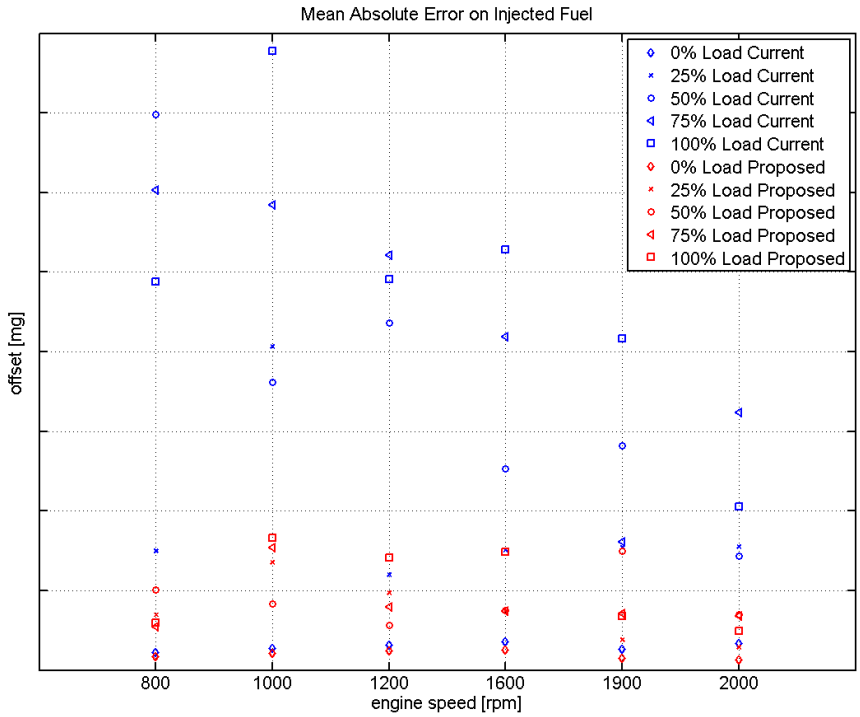

Figure 47 – Mean absolute error on injected fuel: The superior accuracy of the proposed method – red symbols – is evident in every point.

Figure 48 shows the standard deviation of the mean errors shown in Figure 47: the dispersion of the error of the proposed technique – red symbols – is generally lower.

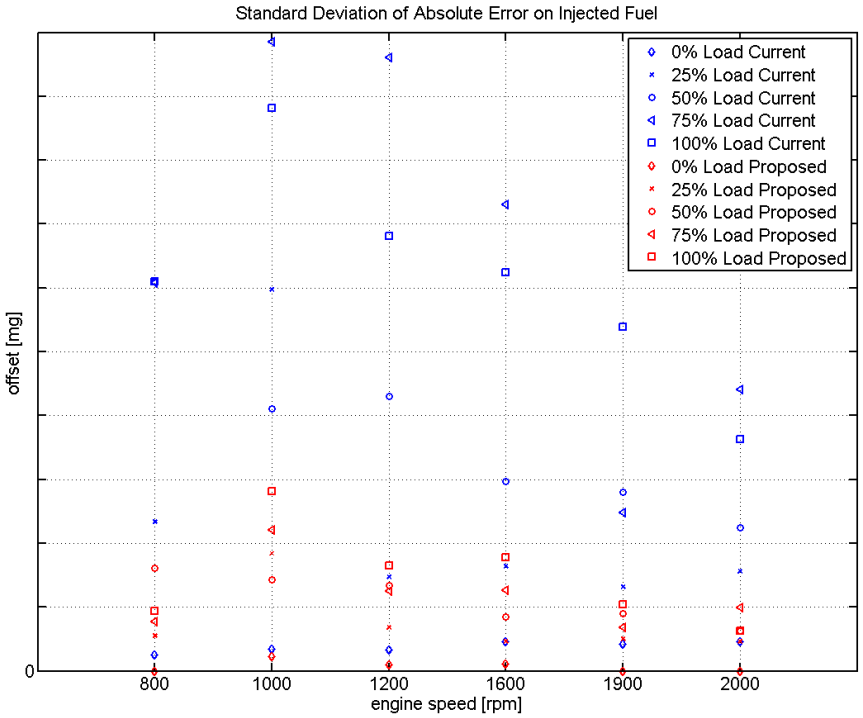

Figure 48 – Standard deviation of the mean absolute error on injected fuel: the dispersion of the error of the proposed technique – red symbols – is generally lower.

The presented measurement technique is solely applicable for approximately rail steady conditions. Complete tests have been conducted for accurately controlled engine operations, therefore the tolerance of the developed method to slow transients in rail pressure has not been determined.

The detection of the method performance to increasing pressure variations per crank shaft revolution would have a significant consequence: The maximum estimation offset considered acceptable would indicate the range of applicability of the proposed method. The maximum $\Delta P_{max}/_{rev}$ found would represent the discerning factor between what can be considered approximately steady and what not.

The current sampling technique implemented today at Scania CV AB has been designed to cover indistinctly both engine steady and transients operations: The accuracy of either cases, however, is necessarily sacrificed in part.

For an acknowledged tolerance of the proposed method to rail pressure transients, an adaptive measurement technique can be implemented. Considering ΔP_{ECU} as the rail pressure difference requested by the ECU during an engine transient:

- If $\Delta P_{ECU} \leq \Delta P_{max}$: The proposed sampling technique can be implemented since it guarantees, as shown in this section, a higher accuracy than the current method.

- If $\Delta P_{ECU} \geq \Delta P_{max}$: The current method has better performances and it might be implemented. An approach expressly designed for rail pressure fast transients, however, is to be further investigated.

The potential improvement following an adaptive measurement technique is unquestionable, but further research needs to be carried out.

8 CONCLUSIONS AND FUTURE WORK

An extensive experimental investigation has been carried out on the high pressure fuel system and several understandings have been achieved. The observed water-hammer instability propagating through the system does not affect the injection process since a mechanical filter in the HPC prevents it from reaching the injector. The flow instabilities at the injector side, therefore, could not be observed. At the rail side, the pressure signature is highly affected by the excitation of the fuel column resonance frequency: The pressure sensor is exposed to significant oscillations affecting the measurement. It has been found that the superposition of injection frequency and pump strokes generates a periodic function with one crank shaft revolution period: The rail pressure signature tends to repeat itself, within a certain degree of accuracy, every three injections for a steady engine operating point.

An attempt to model the transient pressure behaviour in the system has been made: While the frequency content of the phenomenon investigated is correctly interpreted, the results obtained in the time domain diverge significantly in amplitude and phase from the experimental data collected. An improved model should apply more advanced numerical schemes and more detailed modelling for the pump stroke and the injector opening should be implemented also. The results obtained, despite the low accuracy, have shown that fuel temperature and fuel properties have a relevant influence on the system dynamics. No major variations have been observed for changes in the system volume within the specified tolerances. Due to the low reliability of the developed model, no inference on the pressure signature at the injector side has been possible.

The accuracy of the measurement strategy adopted today at Scania CV AB to estimate the mean rail pressure across an injection has been quantitatively assessed for steady engine operations. The estimated mean pressure has been compared to the measured value: In addition to the rail pressure sensor tolerances, other sources of deviation have been found in the age of data employed, in the dispersion of the samples acquired and in the phase shift between pump strokes and injections. The latter, in particular, appears to have a major impact on the effectiveness of the current sampling technique. The analysis carried out, however, could not undergo a fully validation since a tolerance analysis over the SOI and EOI estimations revealed significant inaccuracies in the detection of the actual start and end of injection.

On the basis of the knowledge acquired over the system, a new promising sampling technique has been designed. An adaptive measurement, capable of changing the estimation process accordingly to the engine operating condition detected, has been proposed. The effectiveness of the proposed strategy has been tested for engine steady operations only, proving better results in terms of pressure estimation and, therefore, better performances in controlling the amount fuel injected, main focus of the presented project. An gain in accuracy over the fuel injection has been achieved. The method tolerance to transients in rail pressure is left for further investigation.

Several questions arise from the presented project. The flow instabilities beyond the HPC should be investigated more, experimentally or numerically, in order to determine if the pressure signature recorded at the pressure sensor location is really representative for the pressure drop at the injector. Better estimations of the actual start and end of injection should be achieved: An accurate knowledge of the injection duration would be beneficial for the proposed sampling method. Finally, further investigation regarding the feasibility of the suggested technique is required: In particular, the detection of its tolerance to pressure gradients is crucial for the application of the adaptive measurement technique proposed.

REFERENCES

[1] Catania, A., Ferrari, A., Manno, M., and Spessa, E., "Experimental Analysis of Transient Flow Phenomena in Multi-Jet Common-Rail Systems," *SAE Technical Paper 2005-24-048,* 2005.

[2] Beierer, P., Huhtala, K., Lehto, E., and Vilenius, M., "Study of the Impact of System Characteristics on Pressure Oscillations in a Common Rail Diesel Fuel Injection System," *SAE Technical Paper 2005-01-0910,* 2005.

[3] Zhang, Z., Zongxuan, S., "Rotational angle based pressure control of a common rail fuel injection system for internal combustion engines," *American Control Conference, 2009. ACC'09.. IEEE,* 2009.

[4] Mulemane, A., Han, J., Lu, P., Yoon, S. et al., "Modeling Dynamic Behavior of Diesel Fuel Injection Systems," *SAE Technical Paper 2004-01-0536,* 2004.

[5] Scania, "Service manual handbook, Category 3 - Fuel and exhaust system," in *Workshop Manual, Scania MultiWeb [6.15.0.1]*.

[6] Li, J., Treusch, C., Honel, B., and Neyrat, S., "Simulation of Pressure Pulsations in a Gasoline Injection System and Development of an Effective Damping Technology," *SAE Technical Paper 2005-01-1149,* 2005.

[7] Catania, A. E., Ferrari, A., Manno, M., & Spessa, E. , "Experimental investigation of dynamics effects on multiple-injection common rail system performance," *Journal of Engineering for Gas Turbines and Power, 130(3),* 2008.

[8] Larock, B. E., Jeppson, R. W., & Watters, G. Z. , Hydraulics of pipeline systems, CRC press, 2010.

[9] Wu, S. F., Hu, Q., Stottler, S., & Raghupathi, R. , " Modelling of dynamic responses of an automotive fuel rail system, Part II: Entire system," *Journal of sound and vibration, 245(5), 815-834,* 2001.

[10] Wylie, E. B., Streeter, V. L., & Suo, L., "Fluid transients in systems," *Englewood Cliffs, NJ: Prentice Hall,* 1993.

[11] Vardy, A. E., & Hwang, K. L. , "A characteristics model of transient friction in pipes," *Journal of Hydraulic Research,* vol. 29(5), pp. 669-684, 1991.

[12] Bergant, A., Ross Simpson, A., & Vìtkovsk, J., "Developments in unsteady pipe flow friction modelling," *ournal of Hydraulic Research,* pp. 249-257, 2001.

[13] Vítkovský, J. P., Lambert, M. F., Simpson, A. R., & Bergant, A., "Advances in unsteady friction modelling in transient pipe flow," in *8th Int. Conf. on Pressure Surges*, Bedford, UK, 2000.

[14] Rennels, D. C., & Hudson, H. M. , Pipe Flow: A Practical and Comprehensive Guide, John Wiley & Sons, 212.

[15] P. K. &. J. A. K. Swamee, "Explicit equations for pipe-flow problems," *Journal of the hydraulics division,* pp. 657-664, 1976.

[16] Ghidaoui, M. S., Zhao, M., McInnis, D. A., & Axworthy, D. H., "A review of water hammer theory and practice," *Applied Mechanics Reviews,* pp. 58(1), 49-76, 2005.

[17] Jorques Moreno Carlos, Stenlåås Ola, Hägglund Tore , "Optimization and control of feed and transfer pumps," Department of Automatic Control, Lund University, Lund, 2014.

[18] E. Rundqvist, "Technical Report 7017081," SCANIA, 2013.

[19] Johansson, T., Stenlåås, O., Thomasson, A., "Virtual Sensors for Combustion Parameters Based on In-Cylinder Pressure," Vehicular Systems, ISY, Linköping University, Linköping, 2015.

[20] J. Wolfe, "Open vs Closed pipes (Flutes vs Clarinets)," UNSW - Sydney , [Online]. Available: http://newt.phys.unsw.edu.au/jw/flutes.v.clarinets.html. [Accessed 15 05 2015].

[21] J. Liljencrants, "End Correction at a Flue Pipe Mouth," Fonema, [Online]. Available: http://www.fonema.se/mouthcorr/mouthcorr.htm. [Accessed 15 05 2015].

[22] Issa, R. I., Gosman, A. D., & Watkins, A. P., "The computation of compressible and incompressible recirculating flows by a non-iterative implicit scheme," *Journal of Computational Physics,* vol. 62(1), pp. 66-82, 1986.

APPENDIX A

This appendix presents the average estimation error of the current measurement technique employed today at Scania CV AB for every operating point tested.

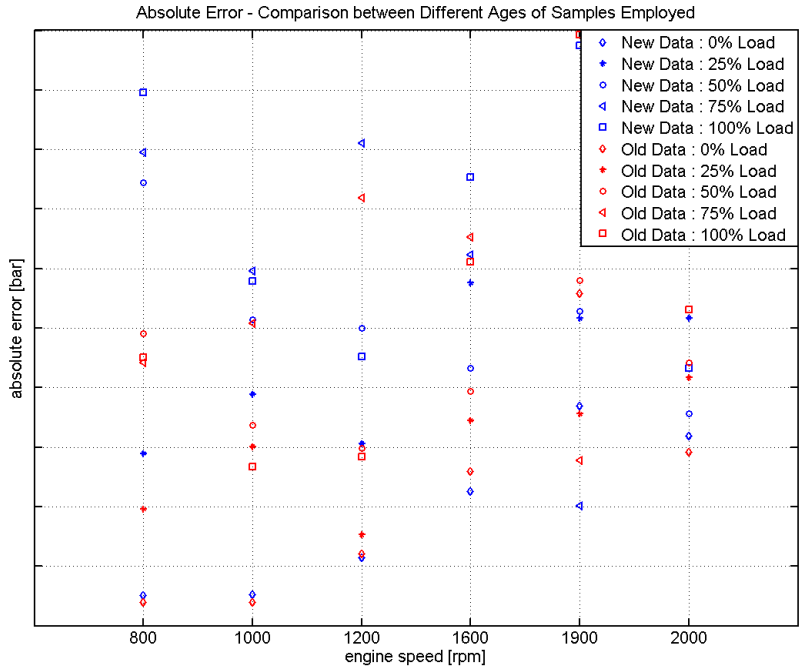

Figure 1 - The mean absolute error in the estimation of the average rail pressure across each injection is shown for every operating point tested. No clear influence of the engine speed over the estimation error is found.

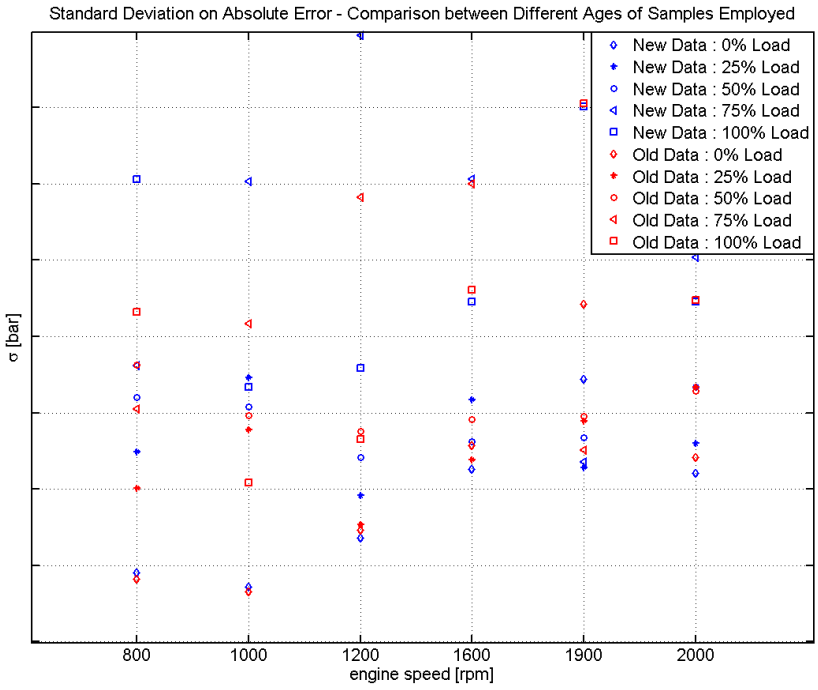

Figure 2 - The standard deviation of the mean absolute error is shown: It is significantly high in general, indicating a high dispersion in the absolute error.

APPENDIX B

This appendix presents the average degree of self-similarity in terms of autocorrelation of the pressure signals acquired for one crank shaft revolution delay.

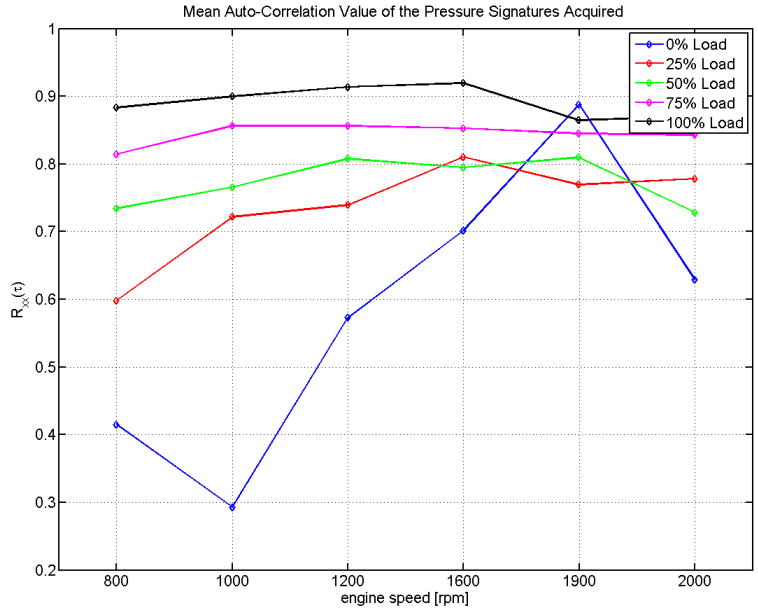

Figure 1 – Mean autocorrelation value after one crank revolution delay for every operating point tested. The self-similarity of the pressure signature acquired remains approximately constant with the engine speed. Note the significant difference in $R_{xx}(\tau)$ for the unloaded case.

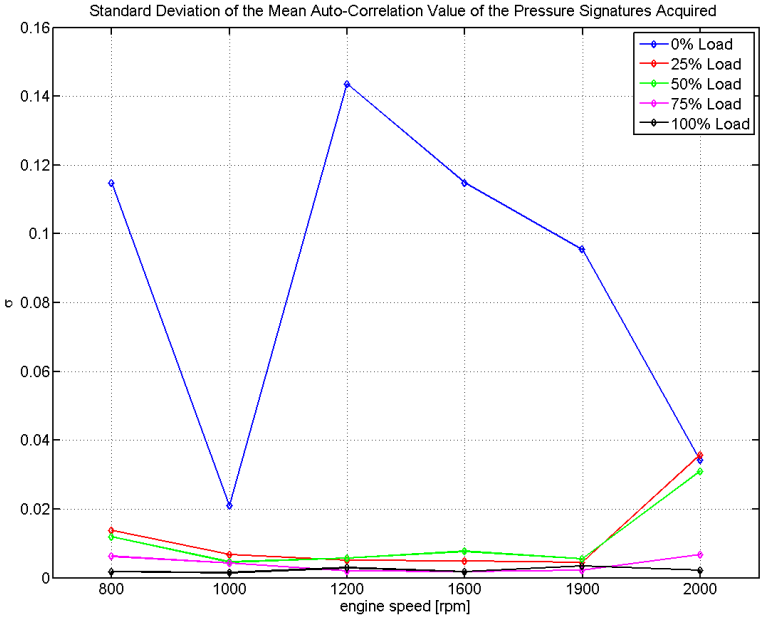

Figure 2 – Standard deviation of the mean autocorrelation value of the pressure signals acquired. The dispersion is approximately constant with the engine speed. Note the significant difference in $R_{xx}(\tau)$ for the unloaded case.